Acta Geochimica (2023) 42:552–571
https://doi.org/10.1007/s11631-023-00599-6

ORIGINAL ARTICLE

Fe-bearing minerals and implications for gold mineralization for the Wangu deposit in Central Jiangnan Orogen

Teng Deng[1,2] · Longyue Zhou[2] · Zenghua Li[1,2]

Received: 29 November 2022 / Revised: 22 February 2023 / Accepted: 24 February 2023 / Published online: 25 March 2023

Abstract Hydrothermal alteration with bleaching of host rocks is the most important prospecting indicator for gold deposits in the Jiangnan Orogen Belt. The alteration has been identified as pre-ore carbonate (siderite)-sericitization and the Fe of siderite in the alteration zone is derived from the host rocks rather than fluids. In addition, such alteration decreases in intensity and width with depth and gold mineralization also occur in the non-bleached rocks, casting doubt on the reliability of the prospecting indicator. Detailed petrographic work and SEM analysis on the Wangu deposit indicate that there are two types of siderites, i.e., Sd1 and Sd2. Among them, Sd1 grains are relatively small and distributed along the planes of unaltered host rocks, while Sd2 grains, only occurring in the altered slates, are commonly larger. Both types of siderites were altered by auriferous fluids, producing porous cores and minerals such as pyrite, quartz, and ankerite. Compared with unaltered parts, the altered parts have lower Fe, but higher U, Pb, and REE. In addition, Sd1 and Sd2 are similar in Mn, Na, V, and Sr concentrations but different in Fe and Mg. The occurrence and geochemical compositions of both siderites indicate that Sd1 could be transformed into Sd2 by pre-mineralization alteration through dissolution-reprecipitation. Chlorite is another important Fe-bearing mineral in the host rocks, and EPMA analysis suggests that it is ripidolite with relatively high Fe contents. Consequently, chlorite can also provide Fe to form the pre-ore carbonate(siderite)-sericitization. Geochemical modeling demonstrates that both ripidolite and siderite can result in sulfidation and therefore gold precipitation. As a result, this study demonstrates that pre-ore alteration with characterized bleaching is not a prerequisite for gold mineralization despite of its prominent features. Due to the presence of Fe-bearing Sd1 and chlorite, gold mineralization could still occur through sulfidation in the unaltered rocks.

Keywords Jiangnan Orogen · Gold precipitation · Wangu deposit · Hydrothermal alteration · Fe-bearing minerals

1 Introduction

Gold precipitation in hydrothermal deposits has generally been interpreted to be caused by fluid boiling, fluid mixing, and fluid-rock interactions (AE Williams-Jones et al. 2009; Wang et al. 2017; Blenkinsop et al. 2020). Among them, fluid boiling is an important mechanism for the rapid precipitation of gold by fractionating H_2S into the vapor phase (Sibson et al. 1988; Henley and Mcnabb 1978; Hurtig and Williams-Jones 2014), and fluid mixing promotes gold deposition by altering the physicochemical conditions of ore fluids (e.g., temperature, pH, oxygen fugacity and S concentrations) (Roberts 1995; Cox et al. 1995; Heinrich et al. 1996; Hu et al. 2017). Fluid-rock interactions can result in hydrothermal alteration and gold mineralization through reduction (Bierlein et al. 1998; Petrella et al.

✉ Teng Deng
dengteng2015@126.com

✉ Longyue Zhou
q13870314721@163.com

[1] State Key Laboratory of Nuclear Resources and Environment, East China University of Technology, Nanchang 330013, China

[2] School of Earth Sciences, East China University of Technology, Nanchang 330013, China

2021), changing pH (Seward et al. 2014), and sulfidation (Su et al. 2009; Pirajno and Yu 2021). The interaction between iron-rich host rocks and Au–S-rich fluids would destroy Au-bearing complexes, resulting in gold precipitation. (Phillips et al. 1984; Stumm and Morgan 1996; Ma et al. 2021).

The Jiangnan Orogenic Belt (JOB), a significant Au-polymetallic metallogenic province in China, hosts more than 250 deposits with about 970 t gold in total (Ni et al. 2015; Liu et al. 2016; Deng and Wang 2016; Xu et al. 2017a, b; Zhang et al. 2018, 2020). The gold deposits of JOB are all hosted in the Neoproterozoic metasediments. Gold mineralization is generally characterized by the bleaching of the host rocks, and this hydrothermal alteration has been used as one of the most important ore prospecting indicators (Xu et al. 2017a). Recent studies demonstrate that this alteration is the pre-ore carbonatization-sericitization, and large amounts of siderite patches form favorable chemical traps for gold mineralization. In addition, these studies also indicate that Fe in siderite is gained from the host rocks rather than hydrothermal fluid (Ma et al. 2021; Xu et al. 2022). However, the original Fe-bearing minerals in the host rocks remain unknown. Moreover, whether carbonatization-sericitization with featured bleaching is a prerequisite for gold mineralization is also unclear, which is critical for further mineral exploration.

The Wangu gold deposit in central JOB is characterized by extensive bleaching alteration of host rocks (Deng et al. 2020), which makes it an ideal research object. The widespread bleaching alteration of the Wangu deposit is due to the formation of siderite which provided a chemical trap for gold precipitation (Ma et al. 2021; Deng et al. 2017, 2020; Zhou et al. 2021). Previous studies have shown that the mineralization temperature of the Wangu is 245 ± 20 °C (Deng et al. 2017, 2020). The major mineralization mechanism is the fluid-rock reaction, while fluid mixing and fluid boiling are weak (Deng et al 2020). This paper aims to: (1) determine the iron minerals of the host rocks through the detailed field and petrographic work, Scanning Electron Microscope (SEM), Raman Spectroscopy, Electron Probe Microanalyzer (EPMA), and Laser Ablation Inductively Coupled Plasma Mass Spectrometry (LA-ICP-MS) analysis; (2) evaluate the association between gold mineralization and hydrothermal alteration and mineral composition of host rocks. Combined with previous research, this study is used to decipher the genetic relationships among iron-rich minerals, bleaching alteration, and gold mineralization as well as its significance for gold exploration in the JOB.

2 Regional geology

The JOB, located at the junction of the Yangtze and Cathaysia blocks of South China, originated from the Neoproterozoic collision of the two blocks (Zhong et al. 2017; Gan et al. 2020; Ma et al. 2021). The rocks of the JOB consist of Early–middle Neoproterozoic volcaniclastic and low-grade metasediments, i.e., the Lengjiaxi and Banxi groups and their equivalents (Xu et al. 2007; Zhao and Cawood 2012; Deng et al. 2020). Multiple structural and magmatic reactivations have been recognized in the JOB from Early Paleozoic to Late Mesozoic, including the Caledonian (Early Paleozoic), Indosinian (Early Mesozoic), and Yanshanian (Late Mesozoic) orogenic movements (Li and Li 2007; Mao et al. 2011; Shu et al. 2015; Zhao 2015; Deng et al. 2019). As one of the most significant gold provinces in China, the JOB hosts hundreds of Au-(polymetallic) deposits (Charvet et al. 1996; Xu et al. 2017a, b; Deng et al. 2017, 2020; Zou et al. 2018). The gold deposits are generally hosted within secondary fractures in the Neoproterozoic low-grade metamorphic rocks (Zhou et al. 1989; Wu et al. 2006; Zhu and Peng 2015; Deng et al. 2017; Xu et al. 2017a; Zhang et al. 2018). Multistage hydrothermal activities caused various wall rock alterations, such as sericitization, silicification, carbonatization, chloritization, and sulfidation (Mao et al. 1997; Xu et al. 2017a; Sun et al. 2018; Liu et al. 2019; Deng et al. 2020; Wang et al. 2020). Different genetic types have been proposed for gold deposits in the JOB, including orogenic, epithermal, intrusion-related, and even sedimentary exhalative (Mao and Li 1997; Gu et al. 2007, 2012; Dong et al. 2007; Deng and Wang 2016; Zhu and Peng 2015). To address the diverse geological and geochemical characteristics, the "intracontinental reactivation type" has been recently proposed for the Au-(polymetallic) deposits in the JOB (Xu et al. 2017a, b).

Northeastern Hunan Province is located in the central segment of the JOB (Fig. 1a). This area is composed of low-grade greenschist-facies metamorphic rocks of the Neoproterozoic Lengjiaxi and Banxi groups, and the Cretaceous red beds, with the local occurrence of the Paleozoic and Tertiary sedimentary rocks (Xu et al. 2006; Gao et al. 2012). The Lengjiaxi Group is composed of low-grade metamorphosed turbidites. The lithologies consist of sandy slates, silty slates, metamorphosed siltstones, and metagreywackes, that are uncomfortably overlain by the Banxi Group, comprising clastic sedimentary rocks including sandstones, slates, phyllites, intermediate–felsic tuffs and conglomerates (Xu et al. 2007; Gao et al. 2011).

This area is characterized by the Late Mesozoic Basin and Range-like tectonic province of South China. It consists of three basins and two uplifts from NW to SE, which

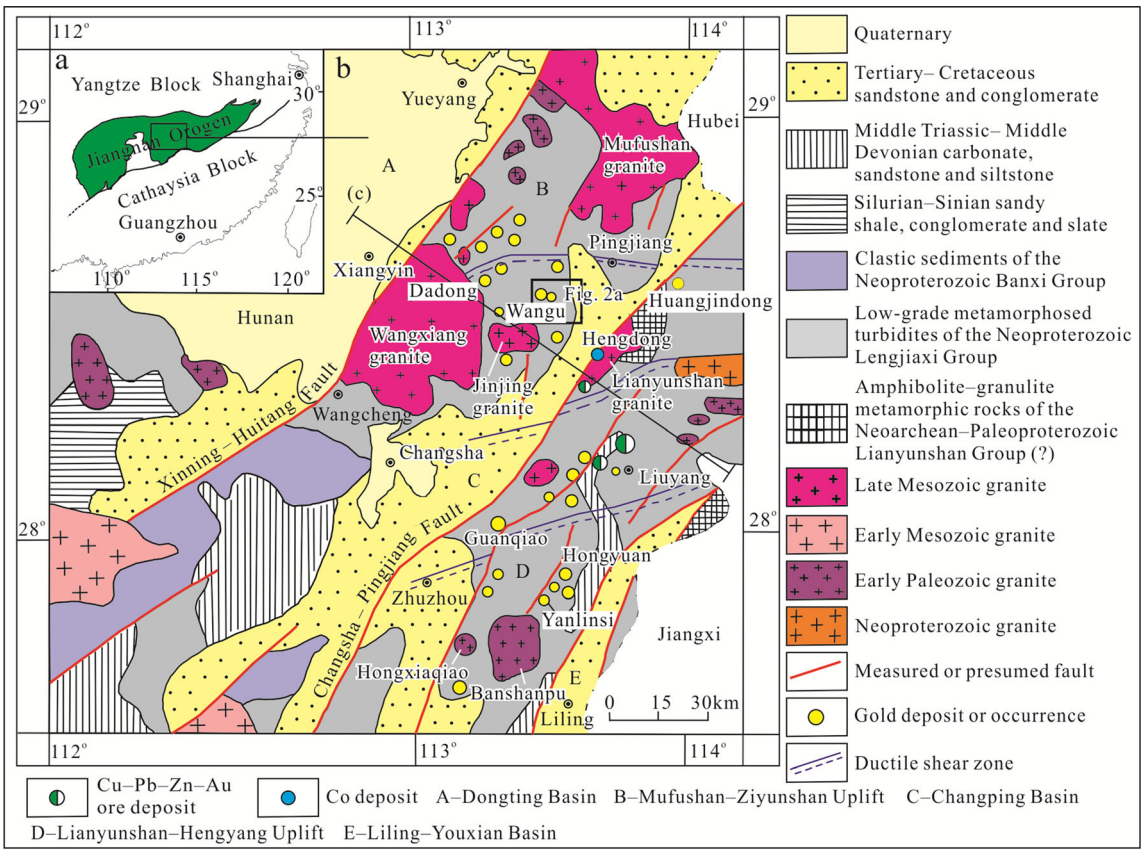

Fig. 1 Simplified tectonic map of South China showing the location of the Jiangnan Orogen (Modified after Sun et al. 2012)

is separated by NE- to ENE-trending strike-slip shear faults, such as the Xinning-Huitang and Changsha-Pingjiang faults (Fig. 1b). In addition, previous studies suggested three EW-trending ductile-shear zones and a series of second-order WNW-trending faults (Fig. 1b) was formed during Early Paleozoic (Xu et al. 2009; Fu 2009).

Granites in the Northeastern Hunan Province were formed in Neoproterozoic, Early Paleozoic, and Late Mesozoic (Fig. 1b) (Xu et al. 2007; Li et al. 2007; Guan et al. 2014). The Neoproterozoic granitoids are S-type and the representative ones are the Getengling, Daweishan, and Changsanbei plutons (Hnbgmr 1988; Deng et al. 2019). The Early Paleozoic granites are I-type, which are represented by the Banshanpu and Hongxia intrusions (Guan et al. 2014). The Late Mesozoic S-type granitoids are the most widely exposed in the area and they generally occur along the regional NE-SW-trending regional faults, such as the Lianyunshan, Jinjing, Wangxiang, and Mufushan intrusions (Jia et al. 2003; Li et al. 2005; Xu et al. 2009; Wang et al. 2014, 2016).

The Northeastern Hunan Province hosts approximately 125 Au(-polymetallic) deposits (Xu et al. 2017a), such as the Wangu, Huangjindong, Yanlinsi, and Liling deposits along the first-order NNE- to NE-trending Chang-Ping Fault. Among them, the Wangu and Huangjindong gold deposits located on both sides of the regional NE-trending Changsha-Pingjiang fault (Fig. 1b) (Deng et al. 2017, 2020; Zhang et al. 2018, 2020; Liu et al. 2019; Sun et al. 2020). The predominant mineralization types are quartz veins, altered slates, and mineralized structural breccias (Zhang et al. 2020; Zhou et al. 2021). Recent studies suggest that the hydrothermal events for the gold deposits in northeastern Hunan mainly took place in the Early Paleozoic and Late Mesozoic (Xu et al. 2017b; Deng et al. 2020; Zhou et al. 2020).

3 Ore deposit geology

The Wangu gold deposit, with a reserve of 85 t Au and an average grade of 6.8 g/t Au, is located within the Mufushan-Ziyunshan uplift and to the northwest of the Changsha-Pingjiang fault (Fig. 1b) (Wen et al. 2016; Deng et al. 2020). The major rocks are the Neoproterozoic and Cretaceous (meta-)sediments. Among them, the Pingyuan Formation of the Neoproterozoic Lengjiaxi Group consists of slates, metamorphic sandstones, and siltstones (Mao et al. 1997), and strikes NW-WNW and dips to NE at

medium angles (Fig. 2a). The Cretaceous Daijiaping Formation, located in the northeast part of the Wangu area, is composed of conglomerates and sandstones (Fig. 2a) (Mao et al. 1997; Deng et al. 2020).

No magmatic intrusions are exposed in the Wangu area (Wen et al. 2016). The major structures in the Wangu deposit are the NE- and E-W- to WNW-trending faults (Fig. 2a). Recent systematic structural analysis has identified five deformation events in the Wangu deposit (Zhou et al. 2021). Among them, the E-W- to ESE- WNW-trending fracture zones were formed during the Early Paleozoic and reactivated during the Early Triassic to Early Cretaceous (Zhou et al. 2021). Gold mineralization took place during the Early Cretaceous reactivation of these fracture zones and was related to the transition from subduction to the rollback of the Paleo-Pacific plate (Sibson 1985; Zhou et al. 2021).

Twenty-four orebodies have been discovered in the Wangu deposit (Deng et al. 2020). The principal ore minerals in the Wangu deposit are arsenopyrite and pyrite, with minor sphalerite, chalcopyrite, scheelite, galena, stibnite, native gold, chalcostibite, and burnonite. The gangue minerals include quartz, siderite, ankerite, chlorite, calcite, and minor sericite (Mao et al. 1997; Ma et al. 2021). In addition, the most distinctive hydrothermal alteration in the Wangu deposit is characterized by the bleaching of the ore-hosting slates (Wen et al. 2016; Deng et al. 2020), with the color transformation from greenish grey to light yellowish gray (Fig. 3a, b). Previous research indicates that the alteration is featured with abundant

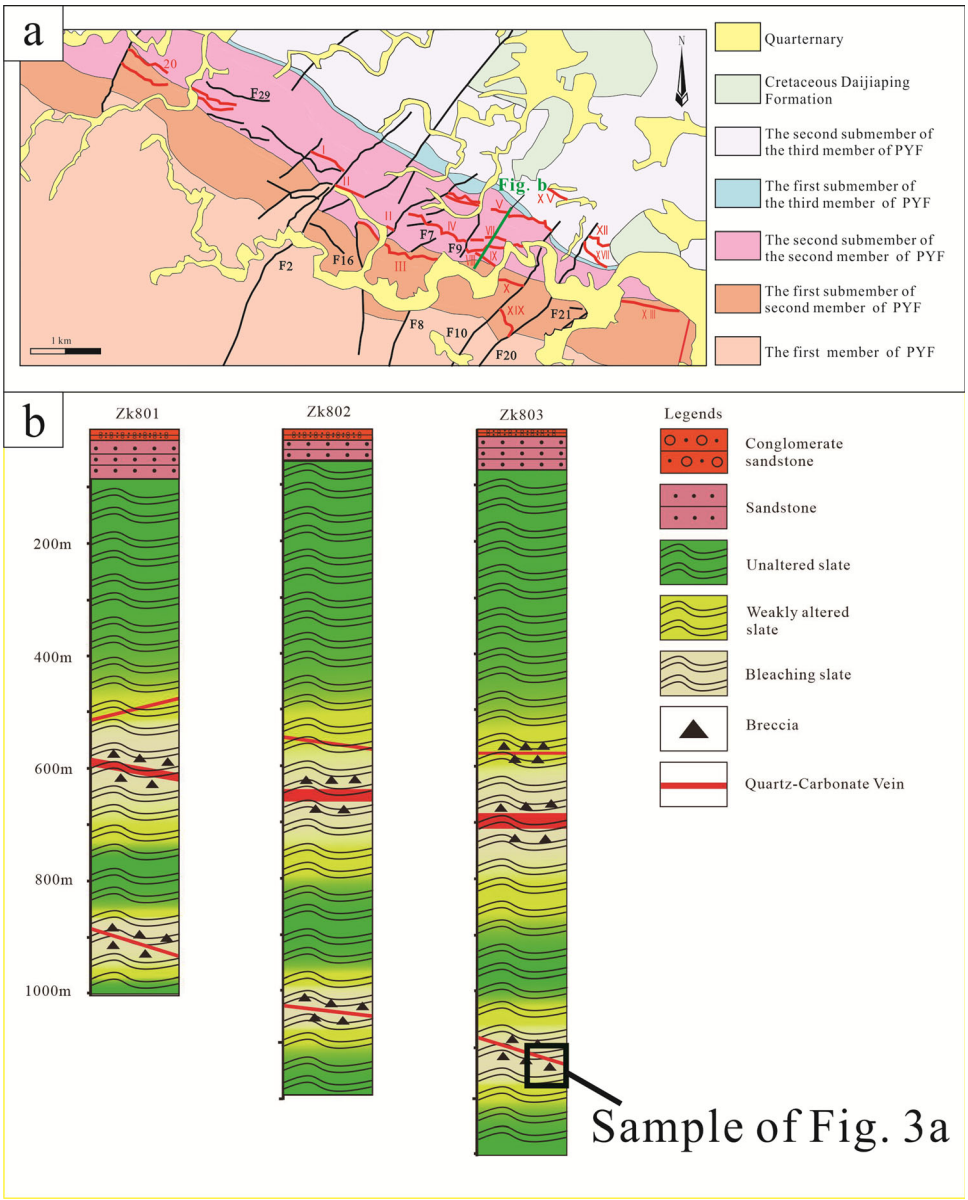

Fig. 2 **a** Geological map of the Wangu gold deposit (Modified after Mao et al. 1997); **b** A cross-section showing ore geological features. The bleaching of slates decreases in both width and extensity with depth

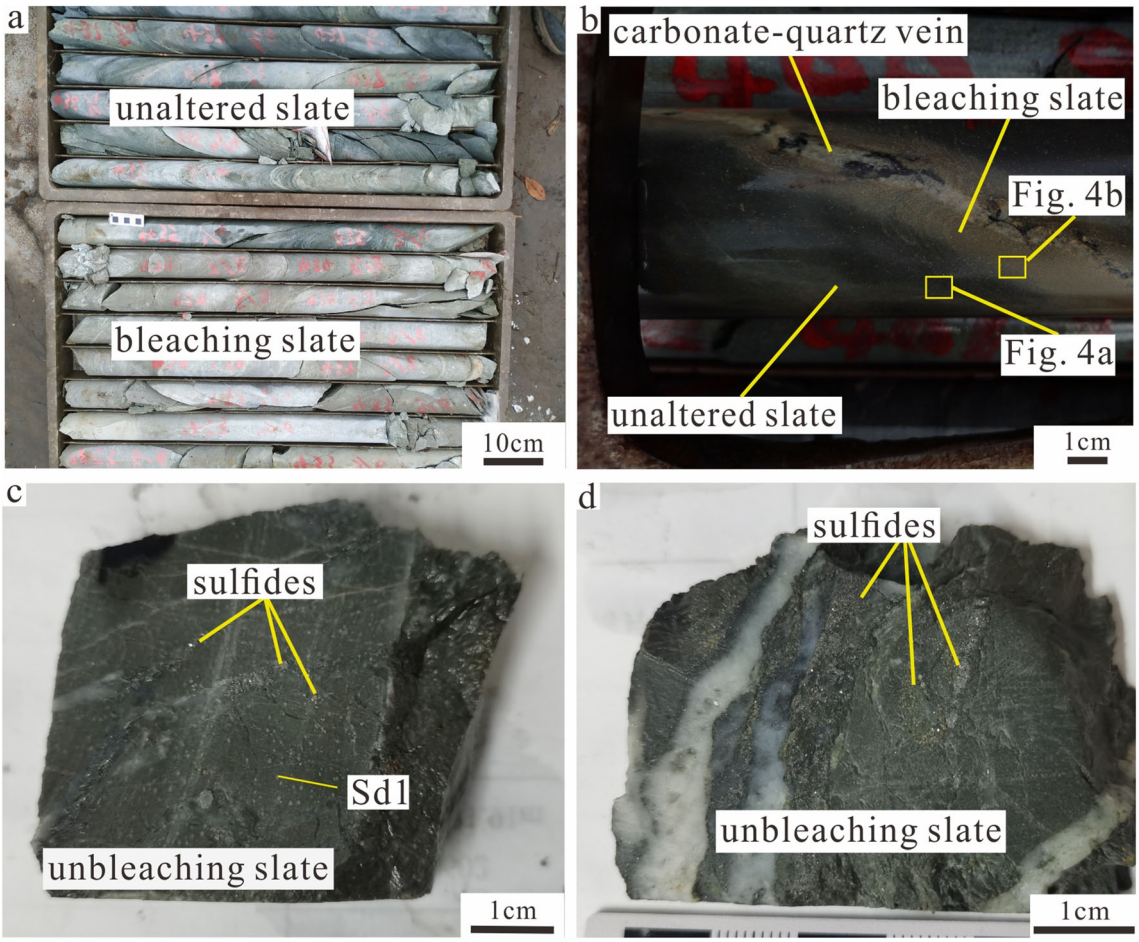

Fig. 3 Photographs and hand specimens from the Wangu gold deposit. **a** Bleached and unaltered slate. **b** The bleaching slate symmetrically enclosing the quartz-carbonate vein; (**c**, **d**) Sulfides in unaltered slates

siderite and sericite (Ma et al. 2021). In addition, arsenopyrite and pyrite are common in altered rocks with distinct bleaching, indicating the ore-forming stage (Fig. 3a, b). However, recent drilling demonstrates that such alteration decreases in both width and intensity in the deeper parts (Figs. 2b, 3c, d).

4 Sample and analytical methods

One hundred samples from drill core ZK803 and sixty-two samples from underground were collected in the Wangu deposit (Fig. 2b). Ten pairs of adjacent samples containing carbonate-quartz veins and bleached, and unbleached rocks were made into polished thin sections for petrography, EPMA and LA-ICP-MS study. Thin section observations were conducted on a Leica DM2700P microscope. Five pairs of adjacent samples, i.e., bleached and unaltered slates were selected for major and trace elemental compositions of siderites. Twelve samples were picked up from the mineralized rocks without bleaching alteration. In addition, another twenty-five samples were collected from auriferous quartz-carbonate veins.

4.1 SEM analysis

The petrography analysis of the chlorite was used by a digital microscope (Leica DM2700P) and scanning electron microscopy (SEM, Zeiss Sigma 300) equipped with Energy Dispersive Spectroscopy (EDS, Oxford AZtec X-Max 80) at the State Key Laboratory of Nuclear Resources and Environment, East China University of Technology. For the SEM analysis on chlorite, carbon coating (10–20 nm thick) was used for the thin sections. The resolution is set at 1.0 nm. The photos were taken by an electron beam exposure machine under the conditions of an accelerating voltage of 5–20 kV and filament current of 24 mA.

4.2 EPMA analysis

Electron probe microanalysis was performed at the State Key Laboratory of Nuclear Resources and Environment, East China University of Technology (ECUT), Nanchang, China. The experimental instrument of the electron probe is JEOL-JXA-8120. The analysis conditions are 20 kV accelerating voltage, 15 nA current, beam spot diameter of 1–2 μm, peak count time of 20 s, and background time of 10 s. The siderite and chlorites are mainly tested. The elements of siderite analyzed including Na, Si, Mg, Al, K, Ca, Fe, Mn, Cr, Ti, Ni, Co, S. The elements of chlorite analyzed including Na, Si, Al, Mg, Ti, Ca, Mn, Fe, Ni, K, Cr. The detection line of most elements is 0.01 wt%.

4.3 LA-ICP-MS analysis

Trace elements of siderite were conducted by LA-ICP-MS at the Guangzhou TuoYan Analytical Technology Co., Ltd., Guangzhou, China. Laser sampling was performed using an NWR-193 laser ablation system. An iCAP-RQ ICP-MS instrument was used to acquire ion-signal intensities. Helium was applied as a carrier gas. Argon was used as the make-up gas and mixed with the carrier gas via a Y-connector before entering the ICP. The spot size and frequency of the laser were set to 30 μm and 6 Hz, respectively, in this study. The energy was 3 J/cm^2. Glass NIST610, NIST 612, and GSE-2G (Reed 1992a, b) were used as external standards for trace element calibration, respectively. Each analysis incorporated a background acquisition of approximately 30 s followed by 40 s of data acquisition from the sample. An Excel-based software ICP-MS-DataCal (Liu et al. 2008) was used to perform offline selection and integration of background and analyzed signals, time-drift correction, and trace element analysis. The elements analyzed include Na, Si, P, Ca, Sc, V, Co, Ni, Cu, Zn, Sr, Y, Nb, Ag, Cd, Sb, Ba, La, Ce, Pr, Nd, Sm, Eu, Gd, Tb, Dy, Ho, Er, Tm, Yb, Lu, Ta, Pb, Th, U.

4.4 LA-ICP-MS trace-element mapping of siderite

Trace elements of siderite were determined using an NWR 193 nm ArF Excimer laser-ablation system coupled to an iCAP RQ (ICPMS) at the Guangzhou Tuoyan Microregion Testing Center, Guangzhou, China. The ICPMS was tuned using NIST 610 standard glass to yield low oxide production rates. 0.7 L/min He carrier gas was fed into the cup, and the aerosol was subsequently mixed with 0.89 L/min Ar make-up gas. The laser fluence was 3.5 J/cm^2, with a repetition rate of 30 Hz and a 5 μm spot size. The laser scan speed was 10 um/s. The raw isotope data were reduced using the "TRACE ELEMENTS" data reduction scheme (DRS). The DRS runs within the freeware IOLITE package of Paton et al. (2011). In IOLITE, user-defined time intervals are established for the baseline correction procedure to calculate session-wide baseline-corrected values for each isotope. Blocks of two standards (one NIST 610 and one NIST 612) and one GSE-2G standard analysis were followed by 5 to 8 unknown samples. For siderite, the following 38 isotopes were measured (with their respective dwell times in milliseconds listed in parentheses):

^{23}Na(5),^{24} Mg(5),^{29}Si(5),^{51} V(5),^{55}Mn(5),^{57}Fe(5),^{59}Co(5),^{88}Sr(5),^{89}Y(5),^{208}Pb(5) and ^{238}U(5) corresponding to a total dwell time of 190 ms.

^{23}Na,^{24} Mg,^{29}Si, ^{51} V,^{55}Mn,^{57}Fe,^{59}Co, ^{88}Sr,^{89}Y, ^{208}Pb, and ^{238}U were corrected by GSE-2G (7.55% Fe) synthetic basaltic glass standard that was prepared using material developed by A.T. Meyers (Meyers et al. 1976). All the isotopes were corrected with a semi-quantitative analysis.

4.5 Geochemical modeling

Geochemical modeling was carried out using the Geochemist's Workbench® (GWB) software package (Bethke 2005, 2006, 2007). Thermodynamic data was modified based on thermo.com. v8. r6 + database, with the addition of As-, Au- and Fe-bearing species from the SUPCRT92 (Johnson et al. 2016; Zimmer et al. 2016). The REACT module was used to simulate the interactions between ore fluids and siderite and chlorite. During the simulations, minerals were suppressed unless they have been reported to occur in the Wangu deposits.

5 Results

5.1 Microscope observation and SEM analysis

Two different generations of siderite can be recognized, i.e., Sd1 and Sd2. Sd1 can be found in the unaltered rocks, and it locally occurs paralleling the planes of the hosting metamorphic rocks. Sd1 grains are generally subhedral–anhedral and have sizes of 100–200 μm (Fig. 4a). In contrast, Sd2 only occurs in the altered rocks characterized by bleaching (Figs. 3a, 4b). Compared with Sd1, Sd2 is much larger (100–300 μm) and more anhedral (Fig. 4b). In addition, chlorite, sericite, and feldspar are also found in the unaltered rocks (Fig. 4c), and chlorite intergrowing with sericite and albite is generally quite small (10–20 μm in length and 5–10 μm in width; Fig. 4d). In the neighboring altered rocks, the amount of chlorite and Sd1 decreased significantly with the production of hydrothermal minerals such as ankerite and Sd2 (Fig. 4e). The common crosscutting of ankerite and Sd2 by gold-bearing sulfides (Fig. 4f) indicates that the two carbonate minerals

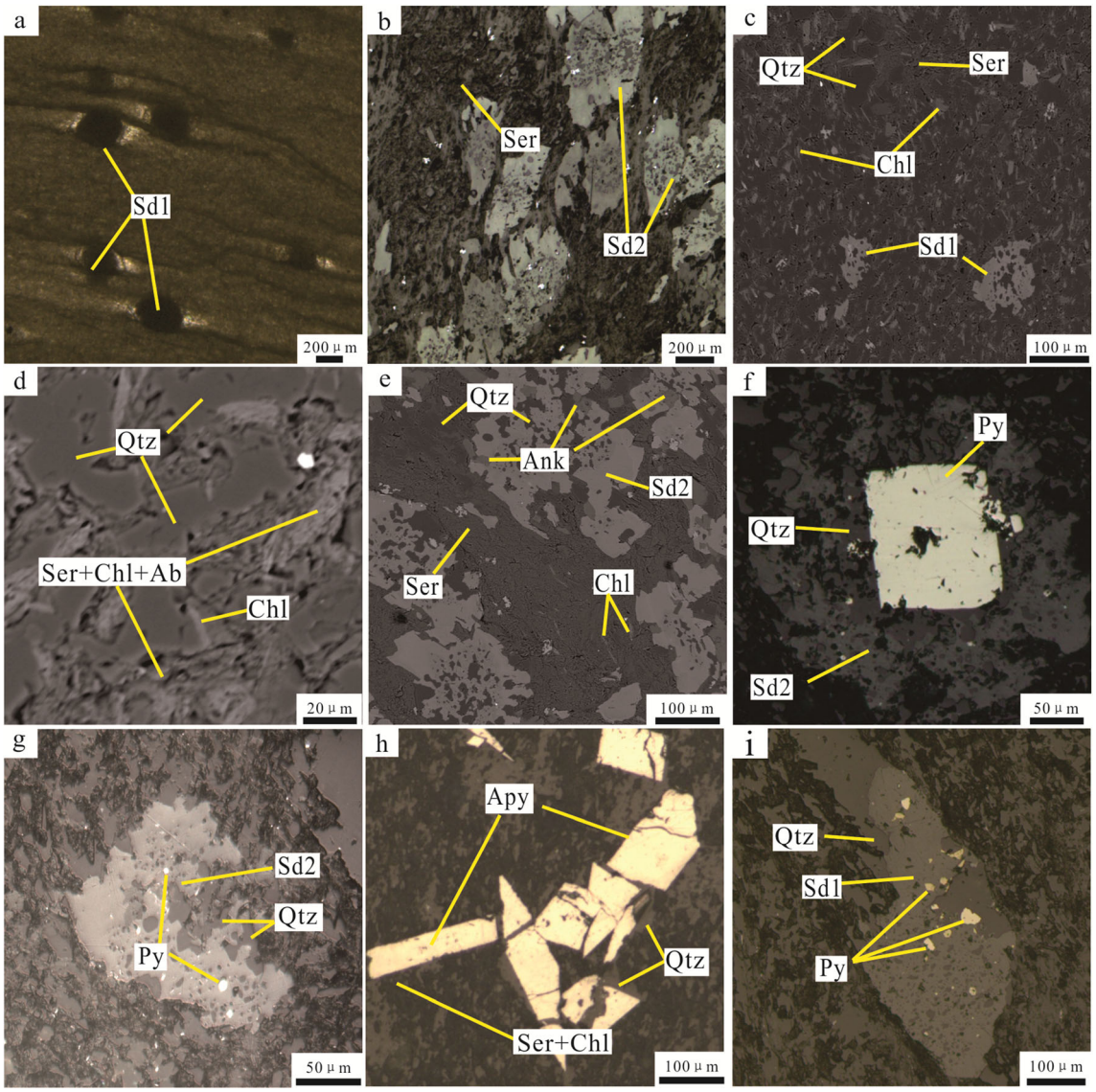

Fig. 4 Photomicrographs of ore bodies and bleached rocks in the field. **a** Sd1 in foliations of unaltered slates. **b** Sd2 occurs in the altered slates. **c**, **d** Quartz, chlorite, Sd1, albite, and sericite in unaltered slates. **e**The bleached slates comprising quartz, chlorite, Sd2, sericite, and ankerite. Sulfides occurring inside altered Sd2 (**f**, **g**), chlorite (**h**), and altered Sd1 (**i**). Ab, albite; Ank, ankerite; Chl, chlorite; Qtz, quartz; Sd, siderite, Ser, sericite; Apy, arsenopyrite; Py, pyrite

are pre-mineralization. Moreover, some Sd2 grains are altered by ore fluids, with the occurrence of quartz, and sulfides in the marginal or interior parts (Fig. 4g).

A large number of sulfides are also present in some unaltered wall rocks (Fig. 3c, d). In these samples, despite the absence of Sd2, sulfides are spatially associated with chlorite. However, due to the fine particle size of the chlorite, it is difficult to discern the clear cross-cutting relationships (Fig. 4h). Similar to Sd2, Sd1 grains are altered by ore fluids with the occurrence of quartz and sulfides (Fig. 4i), indicating that Sd1 and chlorite are also pre-mineralized.

5.2 Major and trace elemental compositions of siderites and chlorite

Samples of Sd1 and Sd2 from the Wangu gold deposit are analyzed by electron probe microanalysis (EPMA) and laser ablation plasma mass spectrometry (LA-ICP-MS) to determine the major and trace elemental compositions and distribution in both altered and unaltered parts (Figs. 5a, 6a). The altered parts are characterized by the occurrence of sulfides and abundant quartz grains (Figs. 5a–c, 6a–c). The analytical results are shown in Tables 1, 2, Figs. 5a–i, 6a–I, and 7a–f. Only data with a total weight percentage

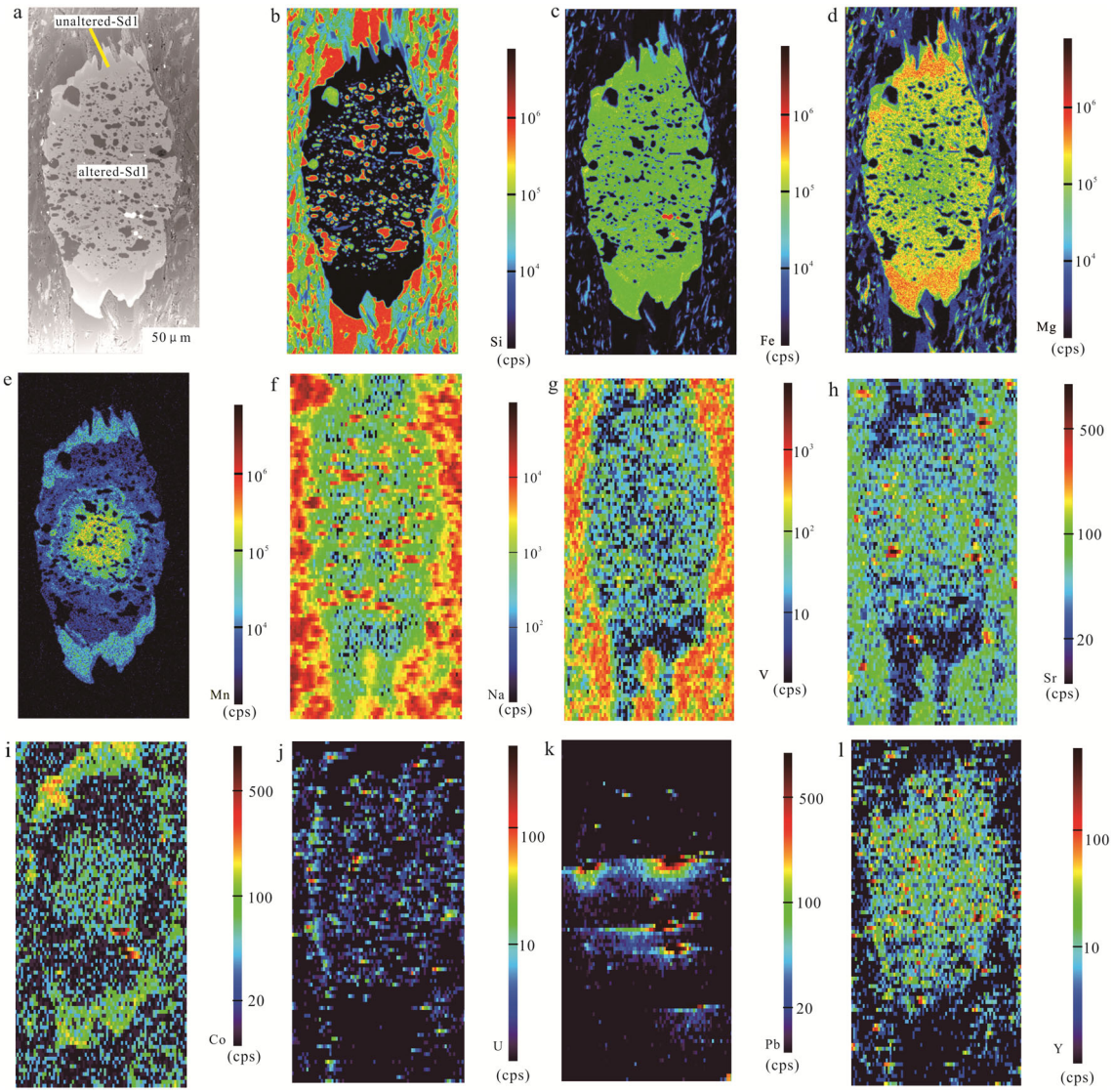

Fig. 5 Elemental mapping of siderite (Sd1) displaying the element distribution in the Wangu deposit

between 56–62 was used for analysis to avoid interference from CO_3^{2-}.

The average FeO content of the altered parts in Sd1 is 40.60–44.66 wt.% (averaging 41.96 wt.%), lower than those of unaltered parts (44.93–47.55 wt.%, averaging 46.23 wt.%) (Figs. 5c, 7a). Compared with the MgO contents of unaltered Sd1 (7.76–11.47 wt.%, averaging 9.55 wt.%), those in the altered parts are higher (10.25–13.20 wt.%, averaging 12.04 wt.%) (Figs. 5d, 7a). In addition, the MgO and FeO contents of Sd1 are negatively correlated (Figs. 5c, d, 7a). The average mass percentages of MnO of Sd1 in the altered parts (1.41–3.99 wt.%, averaging 3.04 wt.%) are relatively enriched compared to those in the unaltered parts (0.64–2.97 wt.%, averaging 2.02 wt.%) (Fig. 7b). In addition, Mg decrease and Mn increase are closely related to the intensity of alteration (Fig. 5d, e). The altered Sd1 has higher mass percentages of NaO (663.00–3920.28 ppm, averaging 2163.66 ppm) than the unaltered Sd1(2.63–993.00 ppm, averaging 554.25 ppm) (Figs. 5f, 7c). For the other transition metals, the contents of Sc, Sr, V, U, and Pb in altered Sd1 are higher than in unaltered Sd1 (Fig. 5g, h, Fig. 7c–d, Fig. 8a), while Co content in the altered Sd1 is relatively lower (Fig. 5i). The REE of altered Sd1 (31.2–400.4 ppm) is significantly more enriched than the REE of unaltered Sd1 (0.9–29.4 ppm) (Fig. 7e), and the contents of Ho and Y are positively correlated (Fig. 8b). The Y/Ho ratios in altered Sd1 (20.9–37.1 ppm) are similar to those in unaltered Sd1 (20.9–28.5 ppm), while the altered Sd1 has much higher La/Yb ratios (increasing from 0.2–0.9 to 0.2–33.3) (Fig. 7f).

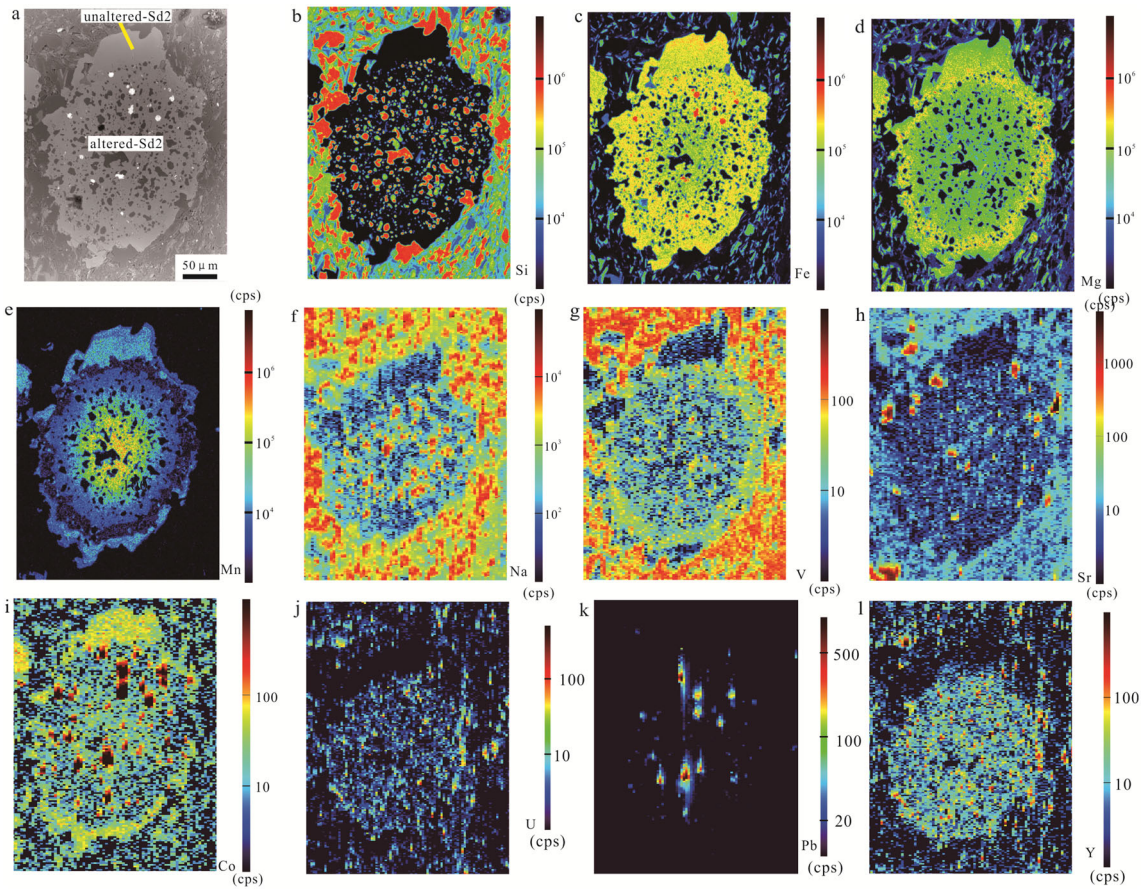

Fig. 6 Elemental mapping of siderite (Sd2) displaying the element distribution in the Wangu deposit

The mass percentages of FeO of the altered parts in Sd2 are 37.69–44.53 wt.% (averaging 40.62 wt.%), while those of the unaltered parts are commonly higher (41.62–44.97 wt.%, averaging 43.14 wt.%) (Figs. 6c, 7a). The contents of MgO of the altered parts in Sd2 are 8.95–11.44 wt.% (averaging 9.76 wt.%), lower than those of the unaltered Sd2 (10.10–13.45 wt.%, averaging 11.71 wt.%) (Fig. 7a). Additionally, the MgO contents in Sd2 are positively correlated with its Fe contents (Fig. 6c, d). The average mass percentages of MnO in the altered Sd2 (1.41–9.48 wt.%, averaging 6.71 wt.%) are relatively enriched compared to those in the unaltered parts (0.56–4.42 wt.%, averaging 2.62 wt.%). In addition, MgO contents are positively correlated with Fe contents in the Sd2 (Fig. 6c, d). The mass percentages of MnO of the altered Sd2 (1.41–9.48 wt.%, averaging 6.71 wt.%) are relatively enriched, compared with the unaltered Sd2 (0.56–4.42 wt.%, averaging 2.62 wt.%) (Fig. 7b). Similar to Sd1, the decrease in Mg and increase in Mn in altered Sd2 are also closely associated with the degree of alteration. (Fig. 5d, e). The average contents of Na_2O of the altered Sd2 are higher than those in the unaltered parts (Fig. 7c, f). In addition, the contents of Sc, Sr, V, U, and Pb in altered Sd2 are relatively higher compared to those in unaltered Sd2 (Figs. 6g, h, 7c, d, Fig. 8a), whereas the Co contents in the altered Sd2 is lower (Fig. 6i). Moreover, the REE of altered Sd2 (18.2–619.1 ppm) is more enriched than those of unaltered Sd2(2.0–32.3 ppm) (Figs. 7e, 8a), and the Ho and Y contents are positively correlated (Fig. 8b). The Y/Ho ratios in altered Sd2 (22.6–26.2 ppm) are similar to those in Sd2 (23.0–29.0 ppm), while the altered Sd2 has much higher La/Yb ratios (increasing from 0.1–0.4 to 0.1–44.0) (Fig. 7f).

In both Sd1 and Sd2, the altered parts have higher in Mn, Na, Sc, Sr, V, U, Pb, and REE, but lower in Fe and Co (Figs. 7, 8a, b). In addition, the contents of Mn in the unaltered parts are similar. In the unaltered parts, the Mn, Na, V, and Sr contents in Sd1 and Sd2 are similar (Figs. 5e–h, 6e–h), but Sd1 generally contains more Fe (Fig. 7a) and less Mg (Fig. 7a). For the altered parts, Sd1 and Sd2 have similar Mn, Na, V, Sr, Co U, Pb and REE contents (Figs. 5e–i, 6e–i, 7c–f, 8a), but Sd1 is more enriched in Mg and Fe (Fig. 7a) but depleted in Mn (Fig. 7b).

The results of EPMA analyses on chlorites in iron-rich host rocks are shown in Table 3. The errors in the

Table 1 Major elemental compositions (wt.%) of Sd1 and Sd2 analyzed by EPMA

Comment	MgO	Al_2O_3	SiO_2	FeO	MnO	Cr_2O_3	TiO_2	SO_3	P_2O_5	Na_2O	CaO	K_2O	CoO	Total
WG808-KW-10A-A-1	9.02	0.37	0.49	37.69	9.09	0	0.91	0.01	0	0.05	0.71	0.09	0.07	58.49
WG808-KW-10A-A-2	9.11	0.39	1.46	38.64	7.93	0	0.02	0	0	0.18	0.69	0.03	0.05	58.5
WG808-KW-10A-A-3	10.11	0.04	0.08	41.86	4.63	0	0.08	0.01	0	0	0.39	0.01	0.02	57.22
WG808-KW-10A-A-4	9.42	0.11	1.85	40.22	7	0.02	0.06	0.02	0	0	0.44	0.02	0.08	59.23
WG808-KW-10A-A-5	10.26	0.06	0.15	43.14	4.39	0.03	0.46	0.02	0	0.01	0.5	0.01	0.03	59.05
WG808-KW-10A-A-6	10.28	0.03	0.74	41.76	5.6	0	0.06	0	0	0.01	0.45	0.01	0.12	59.06
WG808-KW-10A-A-7	9.76	0.01	0.08	40.21	8.14	0	0.02	0.02	0	0.02	0.52	0	0.05	58.83
WG808-KW-10A-A-8	9.92	0.04	0.15	42.34	4.66	0.02	0.42	0	0	0	0.47	0.02	0.09	58.14
WG808-KW-10A-A-9	8.95	0.04	0.93	38.51	9.29	0	0.4	0	0	0	0.6	0	0.04	58.75
WG808-KW-10A-A-10	9.01	0.02	0.98	38.88	9.18	0.02	0.04	0	0	0	0.83	0	0.07	59.02
WG808-KW-10A-A-11	9.2	0.06	0.24	39.31	8.42	0.03	0.09	0.02	0	0	0.82	0.01	0.05	58.24
WG808-KW-10A-A-12	11.13	0.15	0.27	43.5	3.65	0	0.02	0.01	0	0.02	0.3	0.04	0.11	59.2
WG808-KW-10A-A-13	11.45	0.01	0.06	44.54	1.41	0	0.02	0	0	0.01	0.18	0	0.01	57.67
WG808-KW-10A-A-14	11.29	0	0.04	44.28	1.92	0	0.03	0	0.01	0.04	0.35	0	0.06	58
WG808-KW-10A-A-15	9.45	0	0.14	40.39	7.89	0	0.03	0.01	0	0	0.5	0	0.1	58.51
WG808-KW-10A-A-16	8.99	0	1.04	38.25	9.49	0.05	0.05	0	0	0	0.86	0	0.09	58.81
WG808-KW-10A-A-17	9.25	0	1.35	39.05	9.03	0	0.08	0	0	0.02	0.81	0	0.13	59.72
WG808-KW-10A-A-18	9.15	0.03	1.07	38.65	9.11	0	0.04	0	0	0.02	0.82	0.01	0.1	58.99
WG808-KW-10A-O-1	10.1	0.03	0.01	44.98	2.75	0	0.03	0.01	0	0.04	0.12	0.02	0.07	58.17
WG808-KW-10A-O-2	11.66	0.02	0	41.63	3.78	0	0	0	0.01	0.03	0.22	0.01	0.04	57.4
WG808-KW-10A-O-3	11.61	0.01	0.03	41.82	4.22	0	0	0	0	0.03	0.3	0.01	0.07	58.1
WG808-KW-10A-O-4	11.7	0	0.05	41.94	3.87	0.01	0.01	0.01	0	0	0.21	0	0.06	57.87
WG808-KW-10A-O-5	11.42	0.02	0.03	42.78	3.44	0.01	0.02	0	0	0.09	0.19	0.02	0.09	58.11
WG808-KW-10A-O-6	12.3	0.05	0.07	43.1	2.15	0	0.04	0.01	0	0.02	0.04	0.04	0.1	57.91
WG808-KW-10A-O-7	10.8	0.04	1.71	44.18	2.34	0.02	0.01	0	0	0.02	0.05	0.03	0.12	59.31
WG808-KW-10A-O-8	11.41	0.01	0.13	43.53	2.07	0	0.01	0.01	0.01	0.03	0.02	0.03	0.09	57.35
WG808-KW-10A-O-9	11.14	0.43	0.63	44.35	2.18	0	0.02	0	0	0	0.04	0.03	0.03	58.84
WG808-KW-10A-O-10	13.08	0.01	0.13	44.23	0.59	0.01	0.01	0	0	0.02	0.17	0	0.05	58.3
WG808-KW-10A-O-11	11.45	0.03	0.01	42.44	4.01	0.04	0.01	0	0	0.01	0.25	0.01	0.05	58.32
WG808-KW-10A-O-12	13.45	0.05	0.26	42.92	1.27	0.03	0.33	0.01	0.02	0.02	0.15	0.02	0.05	58.6
WG808-KW-10A-O-13	12.86	0.43	1.43	42.47	0.57	0	0.41	0.01	0	0.43	0.15	0.01	0.11	58.87
WG808-KW-10A-O-14	11.31	0	0.04	42.67	3.97	0	0.01	0	0	0.02	0.19	0.01	0.05	58.27
WG808-KW-10A-O-15	11.47	0.02	0.1	44.17	2.1	0.04	0.01	0.01	0.02	0	0.07	0	0.06	58.06
WG808-FI-15ABA-A–1	9.19	0.02	0.05	41.89	7.03	0	0.03	0.03	0	0.04	0.58	0.01	0.05	58.92
WG808-FI-15ABA-A–2	9.35	0.18	1.08	41.86	6.91	0.04	0.05	0	0	0.16	0.68	0.01	0.07	60.39
WG808-FI-15ABA-A–3	9.22	0.14	0.62	41.99	6.21	0	0.14	0.07	0	0.04	0.54	0.04	0.06	59.06
WG808-FI-15ABA-A–4	10.69	0	0.18	44.66	1.41	0	0.02	0.01	0.01	0.02	0.37	0	0.06	57.44
WG808-FI-15ABA-A–5	10.25	0.02	2.2	42.61	1.86	0	4.22	0	0	0	0.3	0.01	0.09	61.56
WG808-FI-15ABA-A–6	10.8	0	0.02	43.22	3.55	0.01	0.04	0	0	0.01	0.28	0	0.05	57.98
WG808-FI-15ABA-A–7	12.48	0.03	0.09	41.84	4	0.01	0.03	0.01	0	0	0.29	0	0.06	58.83
WG808-FI-15ABA-A–8	12.21	0	0.05	41.69	3.69	0.02	0.02	0	0.01	0	0.28	0.01	0.05	58.02
WG808-FI-15ABA-A–9	12.51	0.05	0.1	41.11	3.56	0	0.05	0.01	0	0.01	0.3	0	0.1	57.8
WG808-FI-15ABA-A–10	12.86	0.02	0.04	41.61	3.29	0	0.01	0.01	0	0	0.28	0.01	0.07	58.2
WG808-FI-15ABA-A–11	12.69	0.04	0.04	41.18	2.98	0	0.03	0	0.01	0.03	0.26	0.03	0.05	57.33
WG808-FI-15ABA-A–12	12.79	0.03	0.04	40.6	3.01	0	0	0	0	0.01	0.28	0	0.1	56.85
WG808-FI-15ABA-A–13	13.2	0.01	0.09	41.09	3.1	0.02	0.02	0	0	0	0.23	0.02	0.03	57.81
WG808-FI-15AB-O–1	9.14	0.02	0.18	47.2	2.16	0	0.01	0.01	0	0	0.09	0.01	0.1	58.92
WG808-FI-15AB-O–2	10.26	0.01	0.47	44.93	2.23	0	0.01	0	0	0.04	0.06	0.04	0.09	58.16
WG808-FI-15AB-O–3	9.01	0.01	0.1	46.47	2.19	0	0	0.02	0	0	0.06	0.01	0.05	57.92
WG808-FI-15AB-O–4	7.77	0.04	0.63	47.18	2.31	0	0.02	0.01	0	0.04	0.05	0.02	0.06	58.13
WG808-FI-15AB-O–5	9.68	0	0.07	45.76	2.44	0	0.01	0	0	0	0.17	0.01	0.04	58.19
WG808-FI-15AB-O–6	11.47	0.03	0.57	45.48	0.87	0.01	0.12	0.01	0.03	0	0.31	0.02	0.05	58.96
WG808-FI-15AB-O–7	10.22	0.51	0.79	45.08	2.08	0.01	0	0	0	0.06	0.28	0.12	0.09	59.24
WG808-FI-15AB-O–8	9.1	0.02	0.07	46.21	2.59	0	0	0	0.01	0	0.12	0.02	0.07	58.19
WG808-FI-15AB-O–9	7.78	0	0.02	47.55	2.97	0.01	0.01	0	0	0.02	0.35	0.01	0.07	58.8

Table 1 continued

Comment	MgO	Al_2O_3	SiO_2	FeO	MnO	Cr_2O_3	TiO_2	SO_3	P_2O_5	Na_2O	CaO	K_2O	CoO	Total
WG808-FI-15AB-O–10	10.7	0.02	0.12	46.34	0.64	0	0.01	0	0.02	0	0.12	0.01	0.09	58.06
WG808-KW-10A-O-13	12.857	0.428	1.427	42.47	0.567	–	0.412	0.007	–	0.431	0.154	0.008	0.109	58.87
WG808-KW-10A-O-14	11.307	–	0.036	42.67	3.973	–	0.011	–	–	0.021	0.194	0.007	0.046	58.265
WG808-KW-10A-O-15	11.469	0.015	0.103	44.168	2.104	0.037	0.007	0.01	0.016	–	0.071	0.003	0.061	58.064
WG808-FI-15ABA-A–1	9.189	0.018	0.053	41.888	7.03	–	0.027	0.028	–	0.041	0.584	0.014	0.051	58.923
WG808-FI-15ABA-A–2	9.351	0.176	1.083	41.863	6.912	0.037	0.049	–	–	0.164	0.676	0.005	0.073	60.389
WG808-FI-15ABA-A–3	9.22	0.139	0.619	41.989	6.209	–	0.144	0.066	–	0.041	0.54	0.036	0.058	59.061
WG808-FI-15ABA-A–4	10.691	0.001	0.176	44.664	1.411	–	0.019	0.012	0.008	0.023	0.371	0.002	0.063	57.441
WG808-FI-15ABA-A–5	10.25	0.023	2.2	42.612	1.855	–	4.216	0.003	–	–	0.302	0.011	0.085	61.557
WG808-FI-15ABA-A–6	10.8	0.001	0.018	43.223	3.545	0.011	0.038	–	–	0.01	0.283	–	0.051	57.98
WG808-FI-15ABA-A–7	12.478	0.026	0.086	41.837	3.998	0.008	0.032	0.011	–	–	0.291	0.004	0.063	58.834
WG808-FI-15ABA-A–8	12.207	–	0.051	41.685	3.688	0.018	0.02	–	0.005	–	0.282	0.013	0.051	58.02
WG808-FI-15ABA-A–9	12.509	0.052	0.097	41.111	3.557	–	0.046	0.011	–	0.007	0.302	–	0.104	57.796
WG808-FI-15ABA-A–10	12.856	0.024	0.041	41.611	3.286	0.002	0.01	0.008	–	–	0.281	0.006	0.072	58.197
WG808-FI-15ABA-A–11	12.687	0.044	0.037	41.178	2.977	0.002	0.025	–	0.009	0.034	0.259	0.027	0.051	57.33
WG808-FI-15ABA-A–12	12.788	0.027	0.039	40.603	3.006	–	0.003	0.004	–	0.006	0.276	0.004	0.095	56.851
WG808-FI-15ABA-A–13	13.202	0.009	0.092	41.086	3.099	0.024	0.017	0.004	–	–	0.228	0.019	0.032	57.812
WG808-FI-15AB-O–1	9.139	0.022	0.177	47.2	2.159	–	0.012	0.009	–	–	0.09	0.008	0.099	58.915
WG808-FI-15AB-O–2	10.26	0.007	0.473	44.933	2.232	–	0.014	–	–	0.04	0.064	0.044	0.089	58.156
WG808-FI-15AB-O–3	9.006	0.012	0.098	46.467	2.192	–	0.003	0.021	–	–	0.058	0.013	0.053	57.923
WG808-FI-15AB-O–4	7.765	0.035	0.629	47.177	2.314	0	0.022	0.012	0.002	0.037	0.052	0.024	0.059	58.128
WG808-FI-15AB-O–5	9.683	–	0.068	45.762	2.439	0.002	0.01	0.002	–	–	0.173	0.012	0.036	58.187
WG808-FI-15AB-O–6	11.47	0.03	0.568	45.48	0.874	0.01	0.118	0.011	0.025	–	0.306	0.017	0.047	58.956
WG808-FI-15AB-O–7	10.221	0.512	0.793	45.077	2.075	0.008	0.004	–	–	0.058	0.279	0.122	0.091	59.24
WG808-FI-15AB-O–8	9.095	0.016	0.067	46.21	2.585	–	0	–	0.013	0	0.116	0.024	0.065	58.191
WG808-FI-15AB-O–9	7.779	–	0.022	47.551	2.973	0.005	0.008	0.002	–	0.024	0.354	0.007	0.07	58.795
WG808-FI-15AB-O–10	10.7	0.017	0.12	46.344	0.641	–	0.005	–	0.017	–	0.115	0.01	0.089	58.058

"–"Means below detection limit

composition analysis of chlorite are caused by fine particles, complex structures, and micro inclusions containing other minerals. Contaminated chlorite commonly has elevated ($Na_2O + K_2O + CaO$) contents (> 0.5 wt.%), and thus only the chlorite samples with ($Na_2O + K_2O + CaO$) ≤ 0.5 wt.% are considered here (Foster et al. 1962; Inoue et al. 2010). The EPMA analysis value of chlorites is selected between 83 and 95 wt.%. For the analysis samples, the mass percentages of SiO_2, Al_2O3, MgO, and FeO are 20.67–27.77 wt.%, 17.32–22.02 wt.%, 6.20–10.91 wt.% and 28.66–32.23 wt.%, and the mass percentages of Cr_2O_3, Na_2O, TiO, CaO, MnO, NiO, and K_2O are poor, which are 0–0.055 wt.%, 0–0.171 wt.%, 0.035–0.157 wt.%, 0–0.034 wt.%, 0.109–0.257 wt.%, 0–0.104 wt.%, and 0.033–0.413 wt.%, respectively. Chlorite-related parameters are calculated based on 28 oxygen atoms using EPMA data. The values of Si/O_{28} and Fe/O_{28} range from 4.999–5.626 and 4.126–4.477, respectively. As shown in Fig. 9, the chlorites in the host rocks are mostly ripidolite (Fig. 9).

Chlorite, stable under low temperature and low-pressure environments, has structural variability and non-metrological compositions, so the compositions and structures of chlorite are closely associated with the forming temperature. The formula $d_{001} = 14.339–0.115n(Al^{IV})–0.0201n(Fe^{2+})$ was used to calculate the value of d_{001} (Raused-Colom et al., 1991; Nieto et al. 1997), and then used for calculating the formation temperature of chlorite according to the equation T (°C) = (14.379-d_{001}) / 0.001. As shown in Fig. 10 and Table 3, the temperatures of chlorite range between 242–260 °C (5.35 standard error).

5.3 Au precipitation associated with fluid-rock interactions

The chemical components of the systems investigated include Au-Fe-As-Na- Mg–Al–Si–S–C–Cl–H–O. According to the geothermometry from chlorite in this study and arsenopyrite by Deng et al. (2017, 2020), the temperature was set as 250 °C. Ore fluid compositions were used by Ma et al. (2021). The reaction with siderite results in the co-precipitations of Au, pyrite, and arsenopyrite, and the gold concentrations decreased from 80 to ∼ 3 ppb (Fig. 11a).

Table 2 Trace elemental compositions (ppm) of Sd1 and Sd2 analyzed by LA-ICP-MS

Comment	Na	P	Sc	V	Co	Ni	Cu	Zn	Sr	Y	Nb	Ag	Cd	Sb	Ba	La
WG808-F1-15AB-O-1	993	8.63	14.7	2.87	35.7	10.9	0.0104	136	1.78	0.40	0.97	–	0.043	0.038	6.79	0.031
WG808-F1-15AB-O-2	90.4	8.87	13.7	13.4	28.8	17.0	0.20	116	1.35	0.37	10.5	–	0.062	0.51	19.5	0.048
WG808-F1-15AB-O-3	2.63	2.21	27.8	2.79	37.7	17.7	0.043	132	1.12	0.48	0.14	–	0.055	0.046	2.57	0.053
WG808-F1-15AB-O-4	892	122	15.9	13.2	9.38	11.9	0.31	290	52.3	8.02	5.77	0.0078	0.100	0.58	3.79	0.48
WG808-F1-15AB-O-5	794	171	24.0	7.82	4.81	6.41	0.82	215	10.4	10.8	7.66	0.046	0.054	2.42	9.63	1.99
WG808-F1-15AB-A-1	633	178	18.6	9.66	20.6	20.5	1.99	156	9.52	21.0	7.61	0.015	0.055	2.20	15.6	95.0
WG808-F1-15AB-A-2	1866	148	29.8	8.54	2.76	6.93	0.81	165	12.7	11.7	8.60	0.041	–	1.88	11.2	16.0
WG808-F1-15AB-A-3	2298	76.2	34.6	9.27	3.99	5.93	1.71	168	14.0	12.0	10.3	0.026	0.015	0.66	15.8	2.22
WG808-F1-15AB-A-4	3920.28	1.98	23.9	8.98	10.1	13.1	0.86	476	179	110	10.1	0.025	0.018	1.02	15.6	20.2
WG808-F1-15AB-A-5	2100.94	0.051	43.9	21.5	9.84	11.2	0.21	280	28.9	17.7	15.5	–	–	0.63	78.3	1.15
WG808-KW-10A-O-1	650	1020	25.7	11.7	121	41.4	16.3	194	22.7	12.0	12.4	1.14	0.94	32.9	5.80	1.35
WG808-KW-10A-O-2	27.4	6.07	11.4	1.42	26.1	6.60	0.20	318	0.49	1.64	0.68	–	0.17	–	1.03	0.015
WG808-KW-10A-O-3	4.9	4.59	9.39	1.05	49.4	28.4	–	385	0.13	2.06	0.037	–	0.107	–	–	0.013
WG808-KW-10A-O-4	1146	41.1	9.49	8.03	51.6	49.4	0.12	304	2.79	3.71	0.46	0.021	0.061	0.095	3.11	0.084
WG808-KW-10A-O-5	141	6.75	15.4	11.9	41.8	19.8	0.18	241	3.20	1.03	0.33	–	0.014	0.069	42.6	0.031
WG808-KW-10A-O-6	257	9.74	11.6	15.5	43.8	31.2	0.21	274	3.40	3.93	2.54	0.0075	0.027	0.36	41.6	0.073
WG808-KW-10A-A-1	3144	45.1	25.2	8.81	10.9	6.24	1.79	131	7.70	27.4	8.61	0.024	0.014	2.27	8.53	0.46
WG808-KW-10A-A-2	2039	42.2	17.9	13.0	92.8	28.0	15.0	155	6.71	6.28	6.86	2.91	0.21	7.91	11.7	2.68
WG808-KW-10A-A-3	4575	105	19.6	7.34	7.33	4.86	0.68	135	9.78	10.0	5.06	0.024	–	2.41	7.54	0.50
WG808-KW-10A-A-4	14,591.38	0.040	33.5	23.8	20.4	9.40	2.71	261	21.6	16.4	29.2	0.023	0.080	5.43	25.9	1.06
WG808-KW-10A-A-5	12,929.66	0.70	40.6	17.6	34.9	11.6	4.20	258	62.5	23.2	15.5	0.026	0.15	6.55	22.9	8.59
WG808-KW-10A-A-6	1856	191	12.5	24.8	34.2	35.3	0.021	114	7.98	8.70	3.30	0.015	0.053	0.27	24.6	0.49
WG808-KW-10A-A-7	1420	215	24.8	7.04	31.5	11.2	0.18	94.2	8.37	17.2	4.98	0.0077	0.027	0.68	23.4	139
WG808-KW-10A-A-8	1834	64.7	20.0	8.18	33.2	14.5	0.14	110	7.13	8.60	1.19	0.017	–	0.52	20.7	8.59
WG808-KW-10A-A-9	10,186.26	0.061	33.2	23.2	53.8	21.3	0.89	178	18.8	17.3	30.0	0.076	0.0065	1.65	31.3	1.80

Comment	Ce	Pr	Nd	Sm	Eu	Gd	Tb	Dy	Ho	Er	Tm	Yb	Lu	Ta
WG808-F1-15AB-O-1	0.033	0.0029	-	0.041	0.014	0.021	0.0082	0.055	0.019	0.047	0.027	0.18	0.047	0.085
WG808-F1-15AB-O-2	0.14	0.025	0.15	0.029	0.017	-	0.012	0.11	0.0098	0.039	0.025	0.11	0.027	0.90

Table 2 continued

Comment	Ce	Pr	Nd	Sm	Eu	Gd	Tb	Dy	Ho	Er	Tm	Yb	Lu	Ta
WG808-F1-15AB-O-3	0.100	0.020	0.055	0.013	0.0029	0.039	0.0052	0.056	0.016	0.074	0.029	0.27	0.049	0.013
WG808-F1-15AB-O-4	1.04	0.12	0.64	0.33	0.093	0.59	0.18	1.55	0.32	0.96	0.14	1.39	0.23	0.50
WG808-F1-15AB-O-5	4.00	0.55	2.30	0.93	0.15	1.64	0.25	1.78	0.42	1.46	0.24	2.29	0.43	0.67
WG808-F1-15AB-A-1	174	16.8	63.7	9.26	1.45	5.54	0.86	4.22	0.84	2.40	0.43	2.85	0.49	0.63
WG808-F1-15AB-A-2	28.9	3.33	12.0	2.66	0.50	1.95	0.30	2.04	0.56	1.70	0.36	3.01	0.62	0.72
WG808-F1-15AB-A-3	3.67	0.37	1.97	0.76	0.22	0.97	0.21	1.82	0.45	1.73	0.38	3.62	0.69	0.82
WG808-F1-15AB-A-4	47.3	6.62	36.3	14.1	2.96	19.5	3.11	21.2	3.85	10.9	1.50	8.61	1.28	0.86
WG808-F1-15AB-A-5	3.08	0.44	2.31	1.35	0.24	1.82	0.34	2.93	0.74	2.68	0.55	6.17	1.04	1.31
WG808-KW-10A-O-1	2.92	0.51	2.75	1.34	0.38	1.65	0.29	2.09	0.51	1.80	0.37	3.35	0.64	1.11
WG808-KW-10A-O-2	0.059	0.0033	0.0099	0.023	0.011	0.21	0.023	0.17	0.062	0.29	0.073	0.72	0.14	0.052
WG808-KW-10A-O-3	0.028	0.0071	0.0107	0.013	0.0057	0.09	0.020	0.27	0.089	0.34	0.087	1.07	0.20	0.0054
WG808-KW-10A-O-4	0.23	0.019	0.097	0.058	0.034	0.31	0.063	0.62	0.15	0.59	0.11	0.92	0.20	0.044
WG808-KW-10A-O-5	0.038	0.0038	0.011	–	–	0.067	0.0071	0.12	0.041	0.15	0.021	0.41	0.073	0.027
WG808-KW-10A-O-6	0.21	0.0089	0.11	0.038	0.037	0.16	0.074	0.50	0.17	0.79	0.13	1.29	0.21	0.28
WG808-KW-10A-A-1	0.86	0.11	0.61	0.68	0.25	2.31	0.54	4.51	1.09	3.10	0.52	3.88	0.71	0.71
WG808-KW-10A-A-2	5.94	0.68	3.30	0.82	0.14	0.64	0.16	0.83	0.25	1.08	0.21	1.92	0.28	0.56
WG808-KW-10A-A-3	1.06	0.088	0.57	0.24	0.10	0.86	0.18	1.61	0.38	1.36	0.29	2.51	0.41	0.45
WG808-KW-10A-A-4	2.24	0.22	1.54	0.45	0.14	1.27	0.25	2.32	0.57	2.78	0.49	4.61	0.84	2.78
WG808-KW-10A-A-5	19.2	2.57	13.0	4.95	1.13	6.42	0.82	4.71	1.00	2.85	0.58	5.10	0.92	1.39
WG808-KW-10A-A-6	1.33	0.19	1.02	0.73	0.12	0.60	0.13	1.19	0.38	1.11	0.22	1.61	0.28	0.38
WG808-KW-10A-A-7	263	28.8	117	21.6	3.57	13.2	1.24	4.32	0.65	1.76	0.37	3.16	0.53	0.54
WG808-KW-10A-A-8	15.8	1.76	7.38	1.44	0.28	1.14	0.16	1.40	0.31	1.22	0.25	2.51	0.40	0.11
WG808-KW-10A-A-9	4.79	0.68	2.26	0.67	0.17	1.49	0.21	2.39	0.60	2.32	0.47	4.35	0.82	2.39

Comment	Pb	Th	U
WG808-F1-15AB-O-1	0.46	0.16	0.11
WG808-F1-15AB-O-2	0.37	0.45	0.13
WG808-F1-15AB-O-3	0.097	0.098	0.034
WG808-F1-15AB-O-4	1.21	1.54	0.51
WG808-F1-15AB-O-5	119	3.63	1.17
WG808-F1-15AB-A-1	7.30	19.5	1.54
WG808-F1-15AB-A-2	194	7.72	1.59
WG808-F1-15AB-A-3	2.95	4.38	1.48
WG808-F1-15AB-A-4	4.61	13.4	3.05
WG808-F1-15AB-A-5	4.18	7.00	2.72
WG808-KW-10A-O-1	3654	4.79	4.88
WG808-KW-10A-O-2	1.89	0.24	0.21
WG808-KW-10A-O-3	0.010	0.19	0.18
WG808-KW-10A-O-4	0.25	0.94	0.54
WG808-KW-10A-O-5	0.26	0.17	0.10
WG808-KW-10A-O-6	0.44	1.01	0.60
WG808-KW-10A-A-1	16.8	5.19	2.99
WG808-KW-10A-A-2	7541	3.70	1.94
WG808-KW-10A-A-3	5.89	3.75	2.68
WG808-KW-10A-A-4	22.5	8.38	5.88
WG808-KW-10A-A-5	29.6	8.72	4.07
WG808-KW-10A-A-6	0.49	2.22	1.27
WG808-KW-10A-A-7	2.81	44.7	1.59

Table 2 continued

Comment	Pb	Th	U
WG808-KW-10A-A-8	0.95	4.67	1.32
WG808-KW-10A-A-9	1.53	7.90	3.18

"–"Means below detection limit

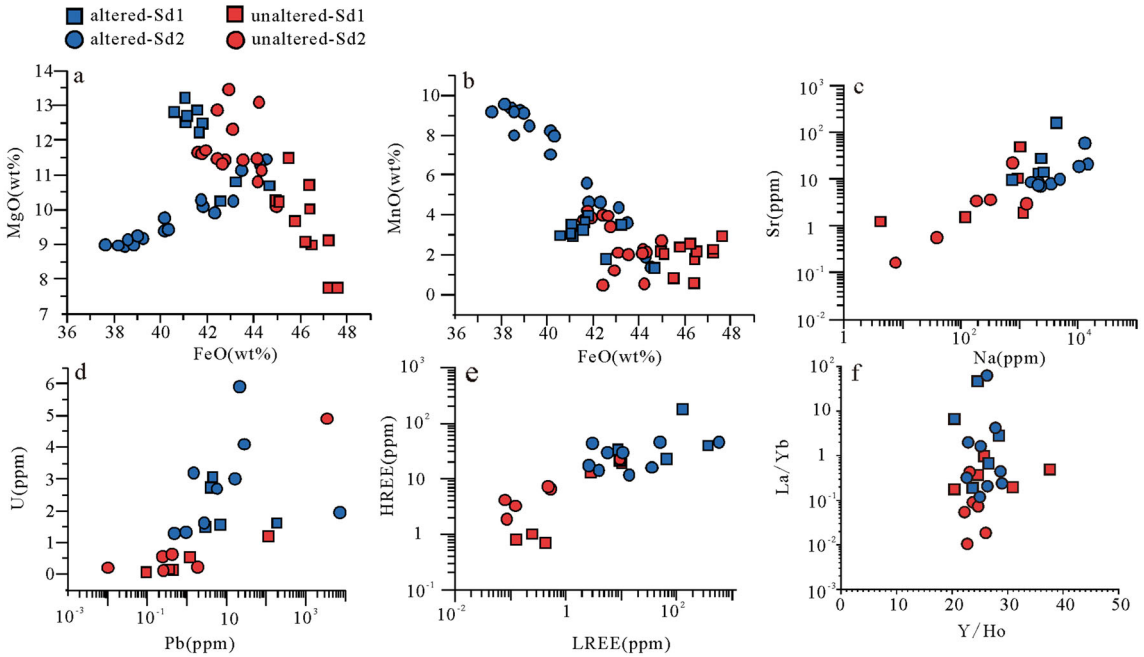

Fig. 7 EPMA and LA-ICP-MS analysis of siderite (altered parts, unaltered parts) showing the values of the elements from altered bleaching slates (Sd1) and unaltered slates (Sd2)

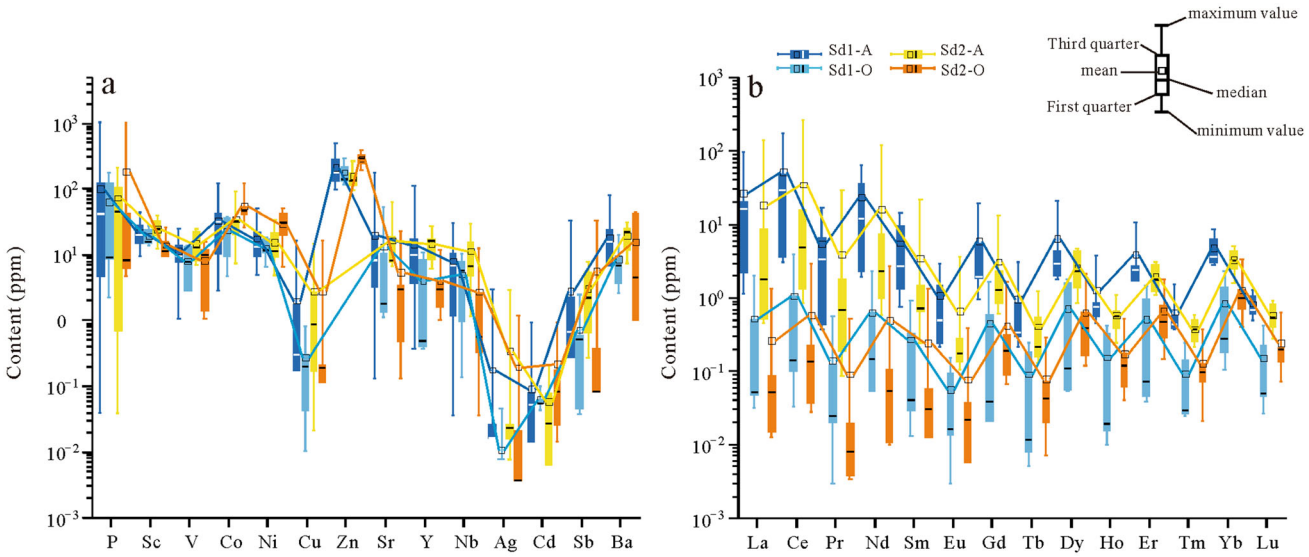

Fig. 8 Box plots of metals and REES of Siderite

Table 3 Major elemental compositions (wt.%) of chlorite analyzed by EPMA

Comment	Na2O	SiO2	Al2O3	MgO	TiO2	CaO	MnO	FeO	NiO	K2O	Cr2O3	Total	Al^{iv}	Fe^{2+}	d_{001}/0.1 nm	T (°C)
13A-1	0.04	25.15	21.45	10.76	0.05	0.01	0.20	31.02	0.03	0.14	0.02	88.86	2.62	5.46	14.13	246.37
13A-2	0.04	23.50	19.97	9.871	0.04	0.01	0.22	32.04	0.07	0.09	0.02	85.85	2.72	6.09	14.12	258.23
13A-3	0.17	24.60	21.13	10.34	0.08	0.02	0.17	31.20	0.07	0.10	0.02	87.89	2.66	5.64	14.13	250.24
13A-4	0.03	23.40	20.15	9.73	0.10	–	0.16	31.61	0.10	0.06	0.04	85.38	2.72	5.99	14.12	257.02
13A-5	0.05	23.67	20.34	9.48	0.06	–	0.14	30.42	0.04	0.21	0.01	84.41	2.64	5.69	14.13	249.63
13A-6	0.04	25.88	22.88	10.92	0.05	–	0.17	30.22	–	0.26	0.05	90.45	2.63	5.07	14.14	242.60
13A-7	0.001	24.90	21.71	9.90	0.04	0.03	0.21	30.08	0.01	0.28	0.05	87.22	2.60	5.28	14.14	243.38
13A-8	0.05	24.23	21.67	9.34	0.16	0.01	0.11	30.20	0.03	0.17	0.05	86.01	2.66	5.38	14.13	247.83
13A-9	0.03	23.36	19.92	9.43	0.04	0.02	0.18	31.39	–	0.10	0.06	84.52	2.67	5.98	14.13	254.34
13A-10	–	23.31	19.95	9.48	0.15	–	0.22	31.28	0.05	0.14	0.02	84.58	2.69	5.96	14.12	255.05
13A-11	0.04	23.00	19.60	9.36	0.07	0.01	0.26	32.16	–	0.04	0.04	84.57	2.73	6.22	14.12	260.42
13A-12	0.05	23.48	19.41	8.92	0.04	0.02	0.15	32.07	0.02	0.03	–	84.20	2.60	6.14	14.13	252.05
13A-13	–	23.87	20.35	9.91	0.06	0.02	0.18	31.35	0.03	0.04	0.03	85.84	2.66	5.83	14.13	252.24
13A-14	0.04	24.24	20.92	9.74	0.06	0.01	0.21	31.96	0.01	0.16	–	87.35	2.67	5.85	14.13	253.02
13A-15	0.03	23.53	20.05	9.36	0.06	0.01	0.13	32.24	–	0.15	0.06	85.61	2.69	6.11	14.12	256.61
13A-16	0.007	23.766	19.7 6	9.8 8	0.09	0.03	0.15	31.78	–	0.05	0.04	85.55	2.64	5.99	14.13	252.86
13A-17	0.012	23.309	19.76	10.03	0.058	0.011	0.102	31.54	0.01	0.066	0.03	84.92	2.71	6.04	14.12	257.33
13A-18	0.027	24.198	20.277	9.62	0.054	0.024	0.083	32.04	0.05	0.2	–	86.57	2.62	5.93	14.13	250.97
13A-19	–	25.087	21.144	10.16	0.041	0.034	0.064	31.80	0.01	0.06	–	88.40	2.59	5.62	14.13	245.97
13A-20	0.008	24.229	19.887	10.52	0.074	0.005	0.07	29.96	–	0.19	0.02	84.97	2.57	5.56	14.14	244.31
13A-21	0.006	24.688	20.8	10.13	0.056	0.007	0.145	29.71	0.07	0.41	0.02	86.04	2.57	5.35	14.14	241.92

"–"Means below detection limit

Gold precipitation occurs with pH increasing to about 5.6 and $fO_2(g)$ values decreasing to about 5×10^{-38} (~ HM-2). Notably, S concentrations in fluids decrease from 10^{-2} to 2×10^{-4} mol/kg (Fig. 11b).

The reaction with ripidolite also results in the co-precipitations of Au, pyrite, and arsenopyrite, and the gold concentrations decreased from 80 to ~ 7 ppb (Fig. 11c). During the initial reactions, no gold precipitates despite the pH increase, and log$fO2(g)$ decrease (Fig. 11c, d). The further reaction leads to Au precipitation with pH generally unchanged and the $fO2(g)$ values decreasing from 6×10^{-37} (~ HM-3) to about 7×10^{-38} (~ HM-2). In addition, S concentrations in fluids decrease from 5×10^{-3} to 9×10^{-4} mol/kg (Fig. 11d).

6 Discussion

6.1 Interpretation of mass transfer during fluid-rock interactions

The altered parts in both Sd1 and Sd2 are characterized by the occurrence of quartz and sulfides (Fig. 4f, g, i), similar to the mineral compositions of the auriferous stage of the Wangu gold deposit (Fig. 4f-i) (Deng et al. 2017, 2020). Consequently, the alteration of Sd1 and Sd2 was generated by fluid-rock interaction with ore fluids. In both types of siderites, the altered parts have lower Fe contents, indicating that siderite is one of the potential sources of Fe that triggered sulfidation (Ma et al. 2021). In addition, the mapping on Co concentration indicates that Co is also incorporated into pyrite grains during alterations (Fig. 5i, k, Fig. 6i, k). Mn contents are enriched in altered siderite

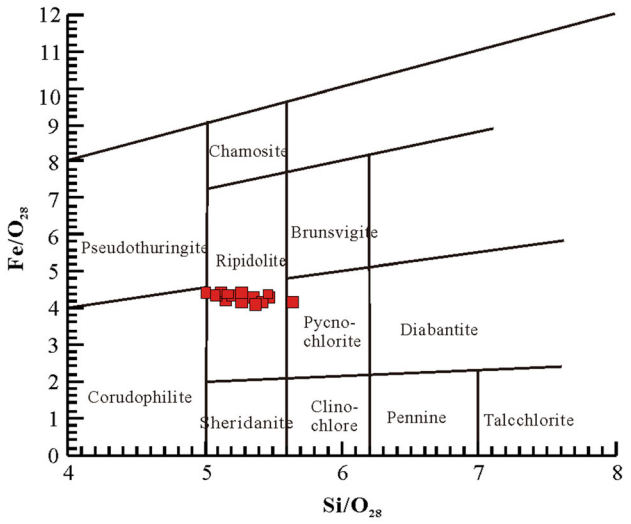

Fig. 9 Plot of chlorites in the Fe^{2+} vs. Si diagram (Modified after Wiewióra & Weiss 1990; Inoue et al. 2010)

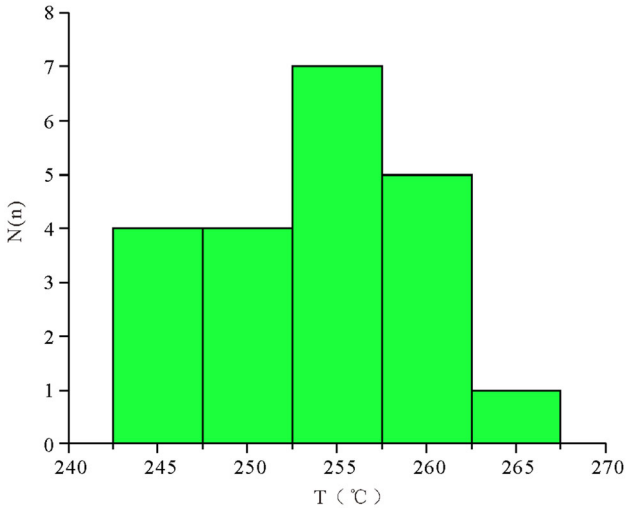

Fig. 10 Columnar section of chlorite

(Figs. 5e, 6e), while Pb contents are also enriched but mostly concentrated in sulfides (Figs. 5k, 6k).

Multiple spots with high Si contents are recognized in the altered siderite, which coincides with the occurrence of quartz inclusions (Figs. 5a, b, 6a, b). Such quartz grains could be possibly incorporated by fluids from host rocks or precipitated by the reactions between ore fluids and siderite. In addition, the pores in the altered siderites have high Na, V, and Sr contents, similar to the host rocks (Figs. 5f-h, 6f-h), indicating they are mainly from host rocks. In addition, the U, Pb, and REE contents in the altered parts of siderite are higher than the unaltered parts (Figs. 5j, l, 6j, l, 7e-f, 8a-b), indicating that they were mainly from the auriferous fluids.

6.2 Implications for gold mineralization

Hydrothermal alterations characterized by the bleaching of host rocks are one of the most important characteristics of the gold deposits in the JOB (Xu et al. 2022; Zhang et al. 2022). Previous studies suggest that such alteration in the Wangu gold is interpreted as carbonation-sericitization with the production of abundant siderite patches (Ma et al. 2021). During the alteration, Fe is from host rocks which aggregate into siderite (Sd2 in this paper) (Ma et al. 2021; Xu et al. 2022), but the original Fe-bearing minerals in host rocks are still unknown. This study shows that the Fe-bearing minerals involved in the unaltered host rocks are mainly chlorite and Sd1. Among them, the chlorite particles in the Wangu gold deposit are generally smaller and have higher Fe content (classified as ripidolite) (Fig. 9). The production of Sd2 from chlorite is associated with the reactions of CO_2-rich pre-ore fluids, which can be explained by the chemical reaction 1. In addition, Sd1 that is locally present in the host rocks can also be aggregated to

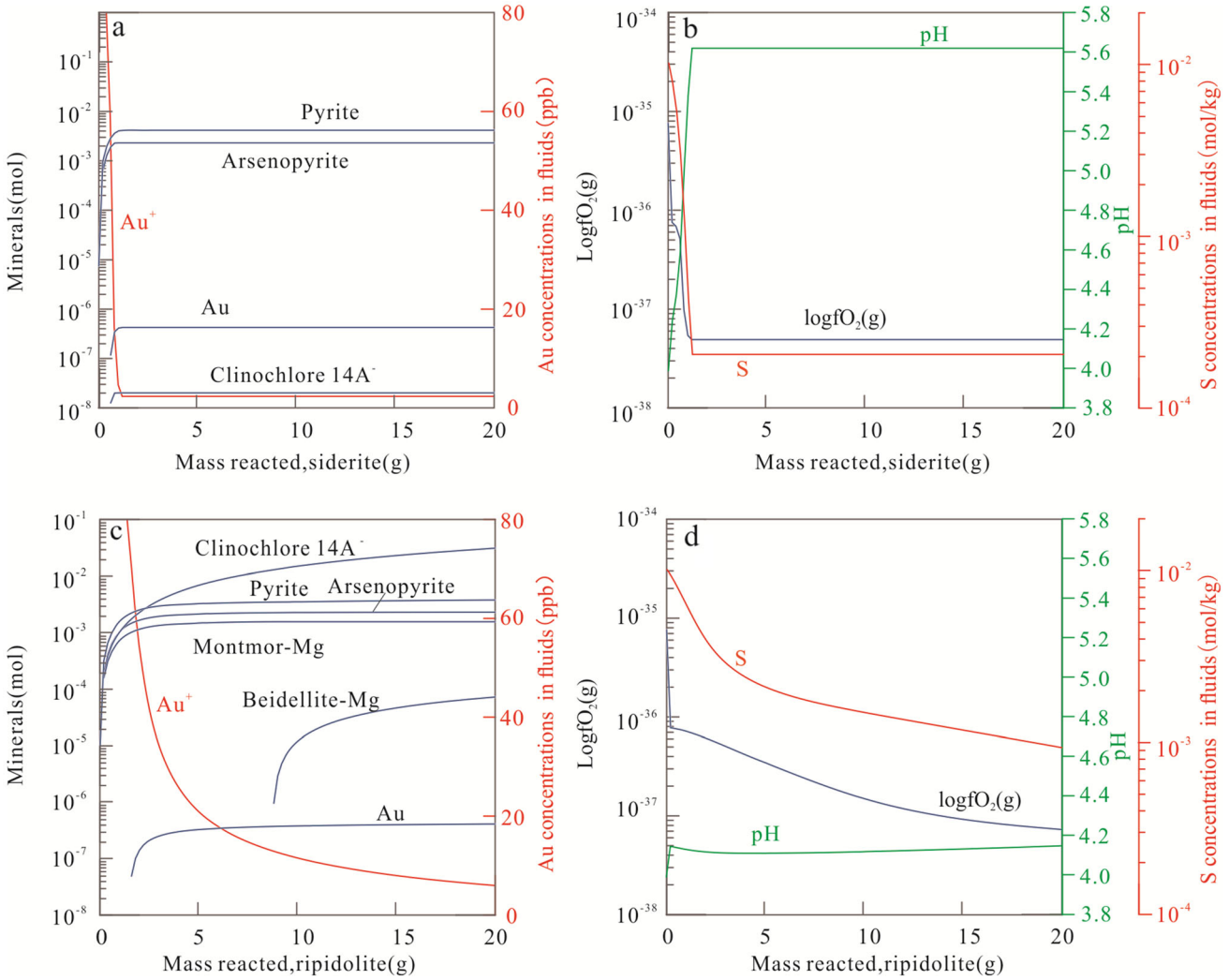

Fig. 11 Fluid-rock interactions with (a-b) siderite (c-d) chlorite (ripidolite)

form larger Sd2 by pre-ore hydrothermal alteration through dissolution-reprecipitation. Consequently, Sd1 and Sd2 show similar contents in Mn, Na, V, Sr, and Co but are different in Mg and Fe.

Ripidolite $(Mg_3Fe_2Al_2Si_3O_{10}(OH)_8) + 14\ H^+ + 2\ HCO^{3-} = 2$ Siderite $(FeCO_3) + 3\ SiO_2(aq) + 2\ Al^{3+} + 12\ H_2O + 3\ Mg^{2+}$

Due to the visible color transformation, the carbonation-sericitization characterized by bleaching has been used as a prospecting indicator for decades (Wen et al. 2016). However, recent deep drilling suggests that such alteration decreases in both intensity and width with the depth (Fig. 2b), resulting in doubting the deep prospecting in the Wangu gold deposit. As demonstrated in this study, Fe is originally sourced from the hosting metasediments, and the pre-ore hydrothermal events caused by carbonation-sericitization only transfer Fe from dissimilated ripidolite into siderite patches (Fig. 4c, e).

Apart from siderite, ripidolite can also trigger sulfidation (Fig. 11), which has been proposed as the major gold precipitation mechanism for the Wangu deposit (Deng et al. 2020; Ma et al. 2021). As indicated by William-Jones et al. (2009), gold solubility is highest when the fluids in near neutral. As shown in Fig. 11b and d, reacting with siderite and chlorite only increases pH to 5.6 and 4.2 respectively, which is favorable for gold dissolution. The most important mechanism here is sulfidation, which leads to co-precipitation of Au and sulfides and therefore drops of the S contents in fluids. This can be evidenced by the occurrence of gold-bearing sulfides. Previous research indicates that deep-sourced fluids transported along the regional Changsha-Pingjiang fault are responsible for the Wangu deposit, so the fluids should be generally consistent within the current prospecting depth (Deng et al. 2017, 2020). In addition, Wen et al. (2016) suggest that geophysical studies demonstrate ore-bearing WNW-

trending faults are well-developed in the deep parts. Combined with thick hosting Lengjiaxi Group, this study indicates that hydrothermal alteration with featured bleaching is not a prerequisite for mineralization for the gold deposits in the JOB, and deep prospecting is potential despite such alteration wanes with depth.

7 Conclusions

1. During syn-ore alteration, Mn, U, REE, and Pb contents increased, but Fe contents decreased, indicating the ore fluid compositions (enriched in Mn, U, REE, and Pb but poor in Fe).
2. Abundant chlorite (ripidolite) and siderite (Sd1) are discovered in the unaltered slates hosting the Wangu gold deposit. These two minerals can provide Fe for pre-mineralization carbonation-sericitization that results in the bleaching of host rocks. Together with the gold mineralization with abundant sulfides in unaltered slates, it is concluded that the pre-ore alteration is not the prerequisite for mineralization for the gold deposits in the Jiangnan Orogen.

Acknowledgements This work was co-founded by the National Natural Science Foundation of China (42002090, 41930428), Jiangxi Double Thousand Plan (SQJH2019XDR), National Key Research and Development Program of China (No. 2018YFC0604200), Open Research Fund Program of State Key Laboratory of Nuclear Resources and Environment, East China University of Technology (No. NRE1915), Open Research Fund Program of Jiangxi Engineering Laboratory on Radioactive Geoscience and Big Data Technology (JELRGBDT202006), International Geoscience Programme (IGCP-675) and Jiangxi province graduate student innovation special fund project (YC2019-S271, DHYC-202001).

Author contribution Teng Deng (First Author): Conceptualization, Methodology, Software, Investigation, Formal Analysis, Writing - Original Draft; Longyue Zhou: Data Curation, Writing - Original Draft; Visualization, Investigation; Zenghua Li: Software, Validation.

Declarations

Conflict of interest On behalf of all authors, the corresponding author states that there is no conflict of interest.

Ethical approval The manuscript has not been submitted to more than one journal for simultaneous consideration. The manuscript has not been published previously (partly or in full), unless the new work concerns an expansion of previous work. A single study is not split up into several parts to increase the quantity of submissions and submitted to various journals or to one journal over time. No data have been fabricated or manipulated (including images) to support our conclusions. No data, text, or theories by others are presented as if they were the authors own. Proper acknowledgements to other works must be given, quotation marks are used for verbatim copying of material, and permissions are secured for material that is copyrighted.

Consent publication The journal may use software to screen for plagiarism. Consent to submit has been received from all co-authors and responsible authorities at the institute/organization where the work has been carried out before the work is submitted.

References

Bierlein FP, Fuller T, Stüwe K (1998) Wallrock alteration associated with turbidite-hosted gold deposits. Examples from the Palaeozoic Lachlan fold belt in central Victoria, Australia. Ore Geol Rev 13(1–5):345–380

Blenkinsop TG, Oliver NHS, Dirks P (2020) Structural geology applied to the evaluation of hydrothermal gold deposits. Rev Econ Geol 21:1–23

Charvet J, Shu L, Shi Y (1996) The building of south China: collision of Yangzi and Cathaysia blocks, problems and tentative answers. J SE Asian Earth Sci 13:223–235

Cox SF, Sun SS, Etheridge MA (1995) Structural and geochemical controls on the development of turbidite-hosted gold quartz vein deposits Wattle Gully Mine, Central Victoria, Australia. Econ Geol 90:1722–1746

Deng J, Wang Q (2016) Gold mineralization in China: Metallogenic provinces, 549 deposit types and tectonic framework. Gondwana Res 36:219–274

Deng T, Xu D, Chi G (2017) Geology, geochronology, geochemistry and ore genesis of the Wangu gold deposit in northeastern Hunan Province, Jiangnan Orogen, South China. Ore Geol Rev 88:619–637

Deng T, Xu D, Chi G (2019) Revisiting the ca. 845–820-Ma S-type granitic magmatism in the Jiangnan Orogen: new insights on the Neoproterozoic tectono-magmatic evolution of South China. Int Geol Rev 61(4):383–403

Deng T, Xu D, Chi G (2020) Caledonian (Early Paleozoic) veins overprinted by Yanshanian (Late Mesozoic) gold mineralization in the Jiangnan Orogen: a case study on gold deposits in northeastern Hunan South China. Ore Geol Rev 124:103586

Dong SW, Zhang YQ, Long CX, Yang ZY, Ji Q, Wang T, Hu JM, Chen XH (2007) Jurassic tectonic revolution in China and new interpretation of the Yanshanian movement. Acta Geol. Sinica 81(11): 1449–1461 (in Chinese with English abstract).

Foster MD (1962) Interpretation of the composition and a classification of the chlorites. U.S. Geological Survey Professional Paper, 414-A: A1–A33

Fu G (2009) Ductile shear deformation in northeastern Hunan Province and their constraint on gold mineralization (PhD Degree Thesis). Guangzhou Institute of Geochemistry, Chinese Academy of Sciences, 123 (in Chinese with English abstract)

Gan C, Wang Y, Barry TL (2020) Late Jurassic High-Mg andesites in the Youjiang Basin and their significance for the southward continuation of the Jiangnan Orogen, South China. Gondwana Res 77:260–273

Gao L, Chen J, Ding X (2011) Zircon SHRIMP U-Pb dating of the tuff bed of Lengjiaxi and Banxi groups, northeastern Hunan: Constraints on the Wuling Movement. Geol Bull China 30:1001–1008 **(in Chinese with English abstract)**

Gao L, Liu YX, Ding X (2012) SHRIMP dating of Cangshuipu Group in the middle part of the Jiangnan Orogen and its implications for tectonic evolutions. Geol China 39:12–20 **(in Chinese with English abstract)**

Guan Y, Yuan C, Sun M (2014) I-type granitoids in the eastern Yangtze Block: implications for the Early Paleozoic intracontinental orogeny in South China. Lithos 206–207:34–51

Gu XX, Schulz O, Vavtar F, Liu JM, Zheng MH, Fu SH (2007) Rare earth element geochemistry of the Woxi W-Sb-Au deposit, Hunan Province, South China. Ore Geol Rev 31(1): 319–336

Gu X, Zhang Y, Schulz O, Vavtar F, Liu J, Zheng M, Zheng L, (2012) The Woxi W-Sb-Au deposit in Hunan, South China: an example of Late Proterozoic sedimentary exhalative (SEDEX) mineralization. J Asian Earth Sci. 57: 54–75

Heinrich CA, Walshe JL, Harrold BP (1996) Chemical mass transfer modelling of ore-forming hydrothermal systems: current practise and problems. Ore Geol Rev 10(3–6):319–338

Henley RW, McNabb A (1978) Magmatic vapor plumes and groundwater interaction in porphyry copper emplacement. Econ Geol 73(1):1–20

HNBGMR (Bureau of geology and mineral Resource of Hunan province) (1988) Regional geology of Hunan province. Geological Publishing House, Beijing: 1722 **in Chinese**

Hu SY, Evans K, Craw D (2017) Resolving the role of carbonaceous material in gold precipitation in metasediment-hosted orogenic gold deposits. Geology 45(2):167–170

Hurtig NC, Williams-Jones AE (2014) An experimental study of the transport of gold through hydration of AuCl in aqueous vapour and vapour-like fluids. Geochim Cosmochim Acta 127:305–325

Inoue A, Kurokawa K, Hatta T (2010) Application of chlorite geothermometry to hydrothermal alteration in Toyoha geothermal system, Southwestern Hokkaido, Japan. Resour Geol 60(1):52–70

Jia D, Hu R, Zhao J (2003) Lithogeochemical characteristics of the Mesozoic granitic intrusion from the Wangxiang area in northeastern Hunan Province and its tectonic setting. Acta Geologica Sinica-Chinese Edition 77:97–103

Johnson CA, Day WC, Rye RO (2016) Oxygen, Hydrogen, Sulfur, and Carbon Isotopes in the Pea Ridge Magnetite-Apatite Deposit, Southeast Missouri, and Sulfur Isotope Comparisons to Other Iron Deposits in the Region. Econ Geol 111(8):2017–2032

Li ZX, Li XH (2007) Formation of the 1300-km-wide intracontinental orogen and postorogenic magmatic province in Mesozoic South China: A flat-slab subduction model. Geol 35(2):179

Li PC, Xu DR, Chen GH (2005) Constraints of petrography, geochemistry and Sr-Nd isotopes on the Jinjing granitoids from northeastern Hunan province, China: implications for petrogenesis and geodynamic setting. Acta Petrologica Sinica 21:921–934

Liao Y (2019). Study on Metallogenic Theory and Prospecting Indicators of Danan Gold Deposit in Wangu Mining Area. World Nonferrous Metals, 13 (in Chinese with English abstract).

Liu YS, Hu ZC, Gao S (2008) In situ analysis of major and trace elements of anhydrous minerals by LA-ICP-MS without applying an internalstandard. Chem Geol 257:34–43

Liu X, Fan HR, Hu FF (2016) Nature and evolution of the ore-forming fluids in the giant Dexing porphyry Cu-Mo-Au deposit, Southeastern China. J Geochem Explor 171:83–95

Liu Q, Shao Y, Chen M (2019) Insights into the genesis of orogenic gold deposits from the Zhengchong gold field, northeastern Hunan Province. China Ore Geol Rev 105:337–355

Ma W, Deng T, Xu D (2021) Geological and geochemical characteristics of hydrothermal alteration in the Wangu deposit in the central Jiangnan Orogenic Belt and implications for gold mineralization. Ore Geol Rev 139:104479

Mao JW, Li YH, (1997) Research on genesis of the gold deposits in the Jiangnan terrain. Geochemica 26(5): 71–81 (in Chinese with English abstract).

Mao J, Pirajno F, Cook N (2011) Mesozoic metallogeny in East China and corresponding geodynamic settings—an introduction to the special issue. Ore Geol Rev 43(1):1–7

Mao J, Li H, Xu J (1997) Geology and genesis of the Wangu gold deposit in Hunan Province, China. Atomic Energy Press, Beijing, pp. 1–133 (in Chinese with English abstract).

Myers AT, Havens RG, Niles WW (1970) Glass reference standards for trace element analysis of geologic materials. Springer, New York

Myint AZ, Wagner T, Fusswinkel T (2022) Calcite trace element geochemistry of Au deposits in the Singu-Tabeikkyin Gold District, Myanmar: Implications for the sources of ore-forming fluids. Ore Geol Rev 145:104892

Ni P, Wang GG, Chen H (2015) An Early Paleozoic orogenic gold belt along the Jiang Shao Fault, South China: Evidence from fluid inclusions and Rb–Sr dating of quartz in the Huangshan and Pingshui deposits. J Asian Earth Sci 103:87–102

Paton C, Hellstrom J, Paul B, Woodhead J, Hergt J (2011) Iolite: freeware for the visualisation and processing of mass spectrometric data. J Anal at Spectrom. https://doi.org/10.1039/c1ja10172b

Petrella L, Thébaud N, Evans K (2021) The role of competitive fluid-rock interaction processes in the formation of high-grade gold deposits. Geochim Cosmochim Acta 313:38–54

Phillips GN, Groves DI, Martyn JE (1984) An epigenetic origin for Archean banded iron-formation-hosted gold deposits. Econ Geol 79(1):162–171

Pirajno F, Yu HC (2021) Cycles of hydrothermal activity, precipitation of chemical sediments, with special reference to Algoma-type BIF. Gondwana Res 100:251–260

Reed WP (1992a) Certificate of analysis: standard reference materials 610 and 611. National Institute of Standards and Technology.

Reed WP (1992b) Certificate of analysis: standard reference materials 610 and 611. National Institute of Standards and Technology

Roberts C (1995) The fosterville project—perseverance exploration Pty., Gold in central Victoria. 125th Anniversary Symposium, Ballarat: 49–51.

Seward TM, Williams-Jones AE, Migdisov AA (2014) The chemistry of metal transport and deposition by ore forming hydrothermal fluids. Treatise Geochem, pp 29–57

Shu LS, Wang B, Cawood PA (2015) Early Paleozoic and Early Mesozoic intraplate tectonic and magmatic events in the Cathaysia Block, South China. Tectonics 34:1600–1621

Sibson R (1985) A note on fault reactivation. J Struct Geology 7:3–6

Sibson RH, Robert F, Poulsen KH (1988) High-angle reverse faults, fluid-pressure cycling, and mesothermal gold-quartz deposits. Geology 16(6):551–555

Stumm W, Morgan JJ (1996) Aquatic chemistry. Wiley, New York

Su W, Heinrich CA, Pettke T (2009) Sediment-hosted gold deposits in Guizhou, China: products of wall-rock sulfidation by deep crustal fluids. Econ Geol 104:73–93

Sun S, Zhang L, Wu S (2018) Metallogenic mechanism of the Huangjindong gold deposit, Jiangnan Orogenic Belt: Constraints from mineral formation environment and physicochemical conditions of metallogenesis. Acta Geol Sinica 34:1469–1483 **(in Chinese with English abstract)**

Sun SC, Yang LQ, Zhang L (2020) In-situ trace elements on pyrite and arsenopyrite of the Zhengchong gold deposit, Jiangnan Orogen: insights for the mineralization mechanism. Ore Geol Rev 122:103486

Wang LX, Ma CQ, Zhang C (2014) Genesis of leucogranite by prolonged fractional crystallization: a case study of the Mufushan complex, South China. Lithos 206–207:147–163

Wang JQ, Shu LS, Santosh M (2016) Petrogenesis and tectonic evolution of Lianyunshan complex, South China: insights on Neoproterozoic and late Mesozoic tectonic evolution of the central Jiangnan Orogen. Gondwana Res 39:114–130

Wang R, Cudahy T, Laukamp C (2017) White mica as a hyperspectral tool in exploration for the Sunrise Dam and Kanowna Belle gold deposits Western Australia. Econ Geol 112(5):1153–1176

Wang C, Shao Y, Zhang X (2020) Metallogenesis of the Hengjiangchong gold deposit in Jiangnan Orogen. South China Ore Geology Reviews 118:103350

Wen Z, Deng T, Dong G (2016) Study on the characters and rules of the ore-controlling structures of the Wangu gold deposit in northeastern Hunan Province. Geotecton Metallog 40:281–294 **(in Chinese with English abstract)**

Wiewióra A, Weiss Z (1990) Crystallochemical classifications of phyllosilicates based on the unified system of projection of chemical composition: II The Chlorite Group. Clay Miner 25(1):83–92

Williams-Jones AE, Bowell RJ, Migdisov AA (2009) Gold in solution. Elements 5(5):281–287

Wilson SA, Ridley WI, Koenig AE (2002) Development of sulfide calibration standards for the laser ablation inductively-coupled plasma mass spectrometry technique. J Anal Atom Spectrosc 17(4):406–409

Wu RX, Zheng YF, Wu YB (2006) Reworking of juvenile crust: element and isotope evidence from neoproterozoic granodiorite in South China. Precambr Res 146(3–4):179–212

Xu D, Chen G, Xia B (2006) The Caledonian adakite-like granodiorites in Banshanpu Area eastern Hunan Province, South China petrogenesis and geological significance. Geol J China Univ 12:507–521 **(in Chinese with English abstract)**

Xu D, Gu X, Li P (2007) Mesoproterozoic-Neoproterozoic transition: Geochemistry, provenance and tectonic setting of clastic sedimentary rocks on the SE margin of the Yangtze Block, South China. J Asian Earth Sci 29:637–650

Xu D, Wang L, Li P (2009) Petrogenesis of the Lianyunshan granites in northeastern Hunan Province, South China, and its geodynamic implication. Acta Petrologica Sinica 25:1056–1078 **(in Chinese with English abstract)**

Xu D, Deng T, Chi G (2017b) Gold mineralization in the Jiangnan Orogenic Belt of South China: geological, geochemical and geochronological characteristics, ore deposit-type and geodynamic setting. Ore Geol Rev 88(565):618

Xu K, Xu D, Deng T (2022) Genesis of altered slate type ores in the Huangjindong gold deposit, Jiangnan Orogenic Belt, South China. J Geochem Explor 241:107047

Xu D, Chi G, Zhang Y (2017a) Yanshanian (Late Mesozoic) ore deposits in China—an introduction to the Special Issue. Ore Geol Rev 88: 481-490.

Zhang L, Yang LQ, Groves DI (2018) Geological and isotopic constraints on ore genesis, Huangjindong gold deposit, Jiangnan Orogen, southern China. Ore Geol Rev 99:264–281

Zhang L, Groves DI, Yang LQ (2020) Utilization of pre-existing competent and barren quartz veins as hosts to later orogenic gold ores at Huangjindong gold deposit, Jiangnan Orogen, southern China. Miner Deposita 55:363–380

Zhao G (2015) Jiangnan Orogen in South China: developing from divergent double subduction. Gondwana Res 27(3):1173–1180

Zhao G, Cawood PA (2012) Precambrian geology of China. Precambr Res 222–223:13–54

Zhong J, Pirajno F, Chen YJ (2017) Epithermal deposits in South China: Geology, geochemistry, geochronology and tectonic setting. Gondwana Res 42:193–219

Zhou X, Sun T, Shen W (2006) Petrogenesis of Mesozoic granitoids and volcanic rocks in South China: a response to tectonic evolution. Episodes 29(1):26

Zhou Y, Xu D, Dong G (2021) The role of structural reactivation for gold mineralization in northeastern Hunan Province South China. J Struct Geol 145:104306

Zhou D, Ye D, Yu D (1989) A preliminary discussion on the genesis of the Mobin quartz vein-type gold deposit in Hunan Province. Mineral Deposits 1.

Zhou Y, Dong G, Xu D (2020) The scheelite Sm-Nd age of the Huangjindong Au deposit in Hunan and its geological significance. Geochimica H202002004 (in Chinese with English abstract).

Zhu YN, Peng JT (2015) Infrared microthermometric and noble gas isotope study of fluid inclusions in ore minerals at the Woxi orogenic Au–Sb–W deposit, western Hunan South China. Ore Geol Rev 65:55–69

Zimmer K, Zhang Y, Lu P (2016) SUPCRTBL: a revised and extended thermodynamic dataset and software package of SUPCRT92. Comput Geosci 90:97–111

Zou S, Zou F, Ning J (2018) A stand-alone Co mineral deposit in northeastern Hunan Province, South China: Its timing, origin of ore fluids and metal Co, and geodynamic setting. Ore Geol Rev 92:42–60